Using a region-specific ice-nucleating particle parameterization improves the representation of Arctic clouds in a global climate model

Astrid B. Gjelsvik[1], Robert O. David[1], Tim Carlsen[1], Franziska Hellmuth[1], Stefan Hofer[1,a],
Zachary McGraw[2,3], Harald Sodemann[4,5], and Trude Storelvmo[1,6]

[1]Department of Geosciences, University of Oslo, Norway
[2]Department of Applied Physics and Applied Mathematics, Columbia University, USA
[3]NASA Goddard Institute for Space Studies, USA
[4]Geophysical Institute, University of Bergen, Norway
[5]Bjerknes Centre for Climate Research, Bergen Norway
[6]Nord University Business School, Nord University, Norway
[a]Now at: School of Geographical Sciences, University of Bristol, UK

Correspondence: Astrid B. Gjelsvik (a.b.gjelsvik@geo.uio.no) and Robert O. David (r.o.david@geo.uio.no)

Abstract. Projections of global climate change and Arctic amplification are sensitive to the representation of low-level cloud phase in climate models. Ice-nucleating particles (INPs) are necessary for primary cloud ice formation at temperatures above approximately -38°C, and thus significantly affect cloud phase and cloud radiative effect. Due to their complex and insufficiently understood variability, INPs constitute an important modelling challenge, especially in remote regions with few ob-

5 servations, such as the Arctic. In this study, INP observations were carried out at Andenes, Norway in March 2021. These observations were used as a basis for an Arctic-specific and purely temperature-dependent INP parameterization, and implemented into the Norwegian Earth System Model. This implementation results in an annual average increase in cloud liquid water path (CLWP) of 70 % for the Arctic, and improves the representation of cloud phase compared to satellite observations. The change in CLWP in boreal autumn and winter is found to likely be the dominant contributor to the annual average increase

10 in net surface cloud radiative effect of 2 Wm^{-2}. This large surface flux increase brings the simulation into better agreement with Arctic ground-based measurements. Despite that the model cannot respond fully to the INP parameterization change due to fixed sea surface temperatures, Arctic surface air temperature increases with 0.7°C in boreal autumn. These findings indicate that INPs could have a significant impact on Arctic climate, and that a region-specific INP parameterization can be a useful tool to improve cloud representation in the Arctic region.

1 Introduction

15 The Arctic has warmed almost four times more than the rest of the world since around 1980, due to anthropogenic climate change (Rantanen et al., 2021). The rapid warming has dramatic consequences for Arctic ecosystems, along with the livelihood of indigenous peoples and other Arctic communities. Amongst the global consequences are sea level rise due to glacier and ice sheet melt, and further temperature increase through loss of bright (high albedo) surfaces such as snow and sea ice. This

20   pronounced warming in the Arctic compared to the rest of the world is known as Arctic amplification (Serreze and Barry, 2011;
Taylor et al., 2022). A number of different climate feedbacks have been proposed to explain it, including the surface albedo
reduction through snow and sea ice loss, confinement of warming to the surface (lapse-rate feedback), increased poleward heat
transport in the atmosphere and ocean, and cloud feedbacks (Forster et al., 2021). However, climate models have been shown
to underestimate the present Arctic amplification (Rantanen et al., 2021; Hahn et al., 2021). The uncertainty in the models arise

25   from uncertainty in the multitude of processes affecting Arctic amplification, including cloud feedbacks (Forster et al., 2021;
Taylor et al., 2022), and their interaction with other processes (Hahn et al., 2021; Taylor et al., 2022).

The changing role of clouds in Earth's radiative budget with warming is arguably the largest uncertainty in determining the
climate sensitivity of the Earth (Forster et al., 2021). Different cloud feedbacks can contribute to both amplifying and damping
radiative forcings, by either trapping more (less) terrestrial radiation from the surface or reflecting less (more) incoming solar

30   radiation. Part of the uncertainty is due to insufficient knowledge on climate feedbacks of cold clouds (Ceppi et al., 2016;
Zelinka et al., 2020; Murray et al., 2021). These can consist of both ice and supercooled liquid water, in which case they
are described as mixed-phase. In the mid- to high-latitudes, low-level clouds can contribute to a significant negative climate
feedback as increasing temperatures will lead to larger fractions of liquid water in the clouds, which will likely increase the
cloud albedo and lifetime (Forster et al., 2021). However, the magnitude of this negative feedback depends on the present

35   supercooled liquid water (SLW) fraction in the clouds (Tan et al., 2016). How this fraction is represented in climate models
is highly diverging, and leads to substantial differences in model climate sensitivity (Zelinka et al., 2020). Models with lower
initial SLW fractions tend to favour a stronger Arctic amplification (Tan and Storelvmo, 2019; Zelinka et al., 2020), making
the SLW fractions of mixed-phase clouds an important area of research for predicting the development of the Arctic and global
climate.

40   In order to represent the SLW fraction correctly in climate models, it is important to correctly represent the concentration of
the available ice-nucleating particles (INPs). These particles are necessary to initiate heterogeneous ice nucleation, occurring
above approximately -38 °C (Kanji et al., 2017). The presence of INPs, therefore, plays an important role in modulating the
concentration of ice crystals in cold clouds. However, the concentration of INPs is highly variable in space and time, and there
is still insufficient knowledge of the sources and properties of these particles (Kanji et al., 2017). For the Arctic, marine organic

45   aerosol particles from ocean biological activity have been presented as a potentially important source of INPs (DeMott et al.,
2016; Wex et al., 2019; Creamean et al., 2019). Other relevant sources are local glacial dust, which Tobo et al. (2019) have
found to have a potentially high ice-nucleating ability, and terrestrial vegetation (Pereira Freitas et al., 2023). More knowledge
on INP concentrations is particularly important in the high-latitudes, where the low-level cold cloud feedback is especially
relevant, but INP concentration measurements are few (Vergara-Temprado et al., 2017; Murray et al., 2021). With a rapidly

50   changing Arctic climate, the sources of INPs are likely also undergoing rapid change, stressing the urgency in understanding
their climate impact.

The objective of this study is to investigate how simulations of Arctic climate, specifically Arctic clouds and radiation, might
change when applying INP concentrations constrained by region-specific observations. We have conducted field measurements
of INPs in Andenes on the Norwegian island Andøy, located north of the Arctic circle. To do this, we used the newly developed
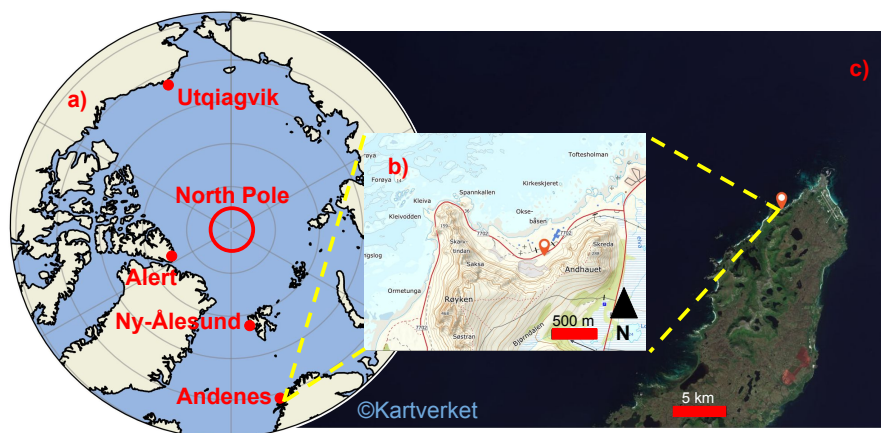
Figure 1. Location of INP measurement site. In panel (a), the position of Andenes, Norway, is shown, together with the other Arctic study regions Alert, Ny-Ålesund, Utqiagvik and the North Pole. In panel (b), the measurement site is marked with a ref pin in the immediate surrounding area, while in panel (c) the site lcoation on Andøy is shown. The maps in (b) and (c) are from ©norgeskart.no (Kartverket, 2022).

55 DRoplet Ice Nuclei Counter Oslo (DRINCO) (based on the instrument DRINCZ David et al. (2019) and FINC Miller et al. (2021) to quantify INP concentrations from collected air samples. The measurements were conducted in March of 2021, a period of frequent outbreaks of polar air masses (cold air outbreaks) reaching the measurement site through northerly winds, similar to the COMBLE campaign in 2020 (Geerts et al., 2022). The observations from Andenes in March 2021 form the basis of a new parameterization for Arctic INP concentrations, which is implemented into the second generation of the Nor-

60 wegian Earth System Model (NorESM2) (Seland et al., 2020b). Previous modelling studies have included parameterizations for marine organic aerosols to better represent INP concentrations in marine environments such as the Arctic in global climate models. The first was implemented by Yun and Penner (2013), and later modelling attempts have shown varying importance of marine organic aerosols for INPs (Huang et al., 2018; Vergara-Temprado et al., 2017; McCluskey et al., 2019). The recent parameterization of Zhao et al. (2021) shows promising ability to reproduce INP concentrations, but more work is still needed.

65 Ours is a more simplified parameterization based only on temperature, but is tailored specifically for the Arctic region, and is restricted to latitudes above 66.5°N. To our knowledge, this is the first attempt at implementing an observation-based INP parameterization for the Arctic, dependent only on temperature, into a global climate model. Building on the master's thesis Gjelsvik (2022), we will demonstrate that such an approach has a substantial effect on Arctic clouds and radiation, and leads to improved representation of Arctic clouds compared to observations.

2 Methods

2.1 Aerosol sampling

70

The field measurements presented here were conducted at Andøya Space (AS) in Andenes, Norway (69°18' N, 16°07' E) from 2021-03-15 to 2021-03-30. The measurements were conducted as part of a joint campaign between the University of Oslo and the University of Bergen.

75 The aerosol sampling site (marked with a ref pin in Fig. 1b) was situated at sea level around two hundred meters from the North-facing shore, and is shielded from the south by mountains that rise approximately 200-400 meters above sea level.

The ambient aerosols were sampled through a 6-meter-high home-built total aerosol inlet. The inlet was heated ($\sim 16°$C) to ensure that all cloud particles were completely evaporated/sublimated before entering the instruments and prevent the build-up of snow and rime from restricting the airflow through the inlet. At the base of the inlet, the flow temperature was monitored

80 (Type K thermocouple recorded by an EL-GFX-TC, Lascar Electronics datalogger) in order to report the aerosol and INP concentrations per standard litre. For sampling, the flow was split to an optical particle counter (OPC; Met One GT-526S) and a three-way ball valve (Model 120VKD025-L, Pfeiffer Vacuum, Germany), which in turn was connected to a high flow-rate liquid impinger (Coriolis-μ, Bertin Instruments, France) and a blower (Model U71HL, Micronel AG, Switzerland). When the Coriolis-μ (described in Sect. 2.1.2) was not sampling, the ball-valve was rotated such that the blower maintained the 300

85 Lmin^{-1} flow through the inlet, as described in Li et al. (2022).

Out of 52 samples in total, 51 are included in this study, excluding one sample measured on 2021-03-19 during a period of substantial wave breaking on the nearby ocean surface, which likely led to sea spray entering the aerosol inlet directly. This sample has estimated INP concentrations, which were clear outliers compared to other samples, and was therefore excluded from the parameterization of Arctic INP concentrations.

90 #### 2.1.1 Aerosol properties

The OPC measured the number of particles per litre of air exceeding certain sizes in bins, i.e. the number of particles with diameter greater than 0.3 μm, 0.5 μm, 0.7 μm, 1 μm, 2 μm and 3 μm. We restrict our analysis to aerosols with diameters of 0.5 μm or larger when comparing aerosol and INP concentrations as this is the cutoff size of the Coriolis-μ, as well as the size that has traditionally been considered most relevant for INPs (DeMott et al., 2010; Kanji et al., 2017).

95 #### 2.1.2 Coriolis setup

The Coriolis-μ collected aerosols for 40 minutes with a flow rate of 300 Lmin^{-1} for a total of 12 m^3 of air per sample for subsequent INP analysis. As the air is sampled by the Coriolis-μ, it rotates inside a cone-shaped flask causing particles larger than ~ 500 nm (aerodynamic diameter) to be scavenged by purified water (W4502, Sigma-Aldrich, USA) due to their inertia. As some of the water evaporates during sampling, additional purified water is pumped into the flask at a fixed rate (e.g. 0.4

mL/min) during sampling. At the end of the sampling period, the resulting water volume of the cone is measured, and the ice-nucleating ability of the particles immersed in the purified water is prepared for further analysis.

2.1.3 INP analysis

The ice-nucleating ability of the collected aerosols was quantified using the DRINCO. DRINCO is based on the DRoplet Ice Nuclei Counter Zurich developed by David et al. (2019), with some updates described in Miller et al. (2021). DRINCO consists of an ethanol chilled bath (Julabo, FP51), a custom PCR tray holder, an LED light array, which is placed in the bath, a webcam (ELP-USB8MP02G-SFV, SVPRO, China) and a bath leveller composed of an optical level sensor (LLC102000, SST, UK) and a peristaltic pump (KAS-S10, Kamoer, China). During an experiment, the temperature of the ethanol bath is cooled at a constant rate of $1°C/min$ and the webcam captures the light emission through a 96-well PCR tray (732-2386, VWR, USA) partially submerged in the bath every $0.25°C$. Each well of the 96-well PCR tray is filled with a 50 μL aliquot of sample (V_a) and the webcam captures the freezing of each aliquot as a decrease in the light intensity due to the lower light transmission through ice relative to water. This results in a frozen fraction (FF) of wells as a function of temperature (FF(T)). To convert this FF to a meaningful INP concentration as a function of temperature (INP(T)), the formulation by Vali (1971) is used. From Vali (1971) the cumulative INP concentration can be calculated as follows:

$$\text{INP}(T) = \frac{-\ln(1 - \text{FF}(T))}{V_a C_{\text{air}}}, \tag{1}$$

where, V_a is the aliquot volume in the PCR tray. The conversion factor C_{air}, following Li et al. (2022), converts this number to the estimated ambient INP concentration in the ambient air as

$$C_{\text{air}} = \frac{V_{\text{air}}}{V_{\text{sample}}} \frac{p}{1013.25\text{hPa}} \frac{273.15\text{K}}{T} \tag{2}$$

where V_{air} is the volume of air sampled by the Coriolis-μ ($\sim 12\,\text{m}^3$), normalized to standard litre using the air flow temperature measurements (T) and the ambient sea level pressure (p) retrieved from MET Norway. V_{sample} is the volume of water in the Coriolis-μ cone at the end of each sample period. The temperature differences between the stated bath temperature and the actual temperature across the PCR tray are accounted for by recording the temperature in the wells in a run using ethanol instead of water in each well, and applying the average temperature offset as a calibration factor.

2.2 Modelling with NorESM2

2.2.1 Model Description

NorESM2 (Bentsen et al., 2013; Iversen et al., 2013; Kirkevåg et al., 2013, 2018; Seland et al., 2020b) is based on the second generation of the Community Earth System Model (CESM2, Hurrell et al., 2013; Danabasoglu et al., 2020). The two models share code infrastructure and many of the same characteristics. As the goal of this modelling study is to investigate the impact of INPs on clouds and radiation, only the atmospheric component of NorESM2 (CAM6-Nor) is used (Seland et al. (2020a)). CAM6-Nor differs from the Community Atmosphere Model of CESM2 (CAM6) in its use of a different atmospheric aerosol

130 module (OsloAero6, Kirkevåg et al., 2018). The module also differs from CAM6 in its improved conservation of energy and momentum, as well as its parameterization of turbulent air-sea fluxes (Toniazzo et al. (2020)). Stratiform cloud microphysics are handled by a two-moment scheme from Morrison and Gettelman (2008). Both CESM2 and NorESM2 have been used to contribute to the sixth and latest generation of the Coupled Model Intercomparison Project (CMIP6; Eyring et al. (2016)).

2.2.2 Heterogeneous ice nucleation in CAM6 and CAM5

135 CAM6 and CAM6-Nor both use a heterogeneous ice nucleation scheme based on classical nucleation theory (CNT), following Hoose et al. (2010). As the primary ice production scheme in CAM6 has a well-documented bug, consisting of an ice number concentration limit that has been shown to prevent heterogeneous nucleation processes from nucleating ice crystals (Shaw et al., 2022), it is unsuitable for studying sensitivities to INP concentration adjustments. Additionally, the CNT scheme calculates ice nucleation based on temperature and the surface area of dust and black carbon aerosols in each time step. However, studies

140 have questioned the relevance of black carbon as an INP (Vergara-Temprado et al., 2018; Kanji et al., 2020; Schill et al., 2020), and marine organic aerosols might be of equal or more importance than dust for the Arctic (Creamean et al., 2019; Wex et al., 2019; Carlsen and David, 2022). Thus, a purely dust and BC-based INP scheme is, either way, less suited for our purposes. Based on these two factors, in combination with the fact that we fail to observe a relationship between INP concentrations and aerosol surface area at Andenes (see Fig. A1), we revert to the ice nucleation parameterizations of CAM5, while simultaneously

145 removing the ice number limit for Arctic mixed-phase clouds. To compensate for the large increase in ice number due to the removal of this limit, secondary ice production is limited to $1000 \ \mathrm{m}^{-3}\mathrm{s}^{-1}$, following Shaw et al. (2022). Ice detrainment is also turned off.

In CAM5, the different heterogeneous ice nucleation pathways are parameterized independently, namely, contact freezing (Young, 1974), immersion freezing (Bigg, 1953) and deposition and condensation freezing (Meyers et al., 1992). Here, we

150 update the parameterization of Meyers et al. (1992) (hereafter: "M92"), active in the temperature range -37°C to 0°C. Since the measured INP concentrations are relevant for the immersion mode, replacing the M92 with our measurements entails excluding deposition and condensation freezing in Arctic mixed-phase clouds. This exclusion is justified by observational studies that found deposition and condensation freezing to be negligible for mixed-phase clouds (Ansmann et al., 2008; Boer et al., 2011; Westbrook and Illingworth, 2013).

155 ### 2.2.3 Model experiments

The performed model experiments conducted in this study are referred to as "M92" and "A21". M92 is a CAM6-Nor set-up with CAM5 heterogeneous ice nucleation schemes. A21 differs from M92 only in replacing the activated ice number produced by the parameterization of Meyers et al. (1992) in the atmospheric column if the latitude of the column exceeds 66.5°N. For these latitudes, the activated ice number concentration is determined by the temperature-dependent parameterization based on

160 INP observations at Andenes (see Fig. 2). For both experiments, we use the atmosphere component with a $2.5° \times 1.875°$ ($\sim 2°$) horizontal resolution, 32 hybrid-pressure layers in the vertical and a "rigid" lid at 3.6 hPa (40 km) (Seland et al. (2020b)). To reduce the required simulation time for the differences due to the different heterogeneous ice nucleation parameterizations to

emerge, both simulations are nudged using ERA-Interim reanalysis data (Dee et al., 2011) of pressure and wind fields. The nudging still allows for the atmospheric component of the model to respond to changes in forcing due to the different parame-

165 terizations used, while having the added benefit of removing climatic variability between the simulations (Dee et al., 2011). As such, we do not investigate the significance of differences between the simulations, as all changes are expected to be a direct result of the changes in the representation of heterogeneous ice nucleation. It is important to note, that as the other components of the model (e.g. ocean, land) are represented using input files, only the simulated temperatures over land and sea ice can respond to energy fluxes from the atmosphere, while sea surface temperatures are fixed to an observed 10-year climatology

170 around the year 2000. The simulations presented here are three years long with an additional three months for model spin up time. The specific simulation period, excluding spin up, is therefore 2007-04-01 to 2010-03-31. The calculation of modelled cloud radiative effect at surface and the top-of-the-atmosphere (TOA), as well as estimated cloud longwave emissivity, is shown in Sect. B2 and Sect. B3, respectively.

2.3 Cloud phase metrics and CALIOP lidar comparison

175 In order to compare the output of our model experiments directly with lidar observations, we use the same method as Shaw et al. (2022) to generate output of SLW fraction for two cloud phase metrics, one for "cloud top" and one for "cloud bulk". These are generated by filtering the overlying cloud optical thickness (COT), first by discarding the uppermost layers with COT < 0.3 to avoid including cirrus clouds and then selecting the highest layer of clouds within the mixed-phase temperature regime, which is categorised as "cloud top". Second, the "cloud bulk" is acquired by selecting all cloud layers with $0.3 < COT$

180 < 3.0. The lidar observations are from NASA's Cloud-Aerosol lidar with Orthogonal Polarization (CALIOP, Winker et al., 2009). The instrument can discriminate spherical water droplets from non-spherical ice crystals in clouds by the ratio of the perpendicular and parallel polarization of the backscatter returns from its laser signal. We use CALIOP data averaged over the observational period $2009\text{-}06\text{-}01 - 2013\text{-}05\text{-}31$. The observations are binned down to a $1° \times 1°$ resolution for comparison with the model output. The SLW fraction is calculated on isotherms from $-40°C$ to $0°C$, with a $5°C$ increment. The observed SLW

185 fraction is calculated as the the ratio of the number of liquid cloud top pixels to the sum of ice plus liquid cloud top pixels, following Bruno et al. (2021). The modelled SLW fraction is calculated as the ratio of cloud liquid surface area density to the sum of liquid and ice surface area densities, based on the method of Tan et al. (2016), which instead used cloud ice and cloud liquid mixing ratios. The data is spatially averaged over the Arctic, for latitudes above $66.5°$ and up to $82°$, which is the northernmost limit of the lidar observations.

190 2.4 Radiative flux observations

The modelled radiative fluxes are compared with observations both for the top-of-the-atmosphere (TOA) fluxes and the surface fluxes in the Arctic. We retrieve TOA fluxes from the Clouds and Earth's Radiant Energy Systems (CERES) Energy Balanced and Filled (EBAF) data product (Loeb et al., 2018), and corresponding uncertainty estimates from NASA (2021). Surface fluxes are retrieved from three different Arctic measurement stations in the Baseline Surface Radiation Network (BSRN); Alert

195 (82°30'N, 62°22'W), Utqiaġvik (71°17'N, 156°47'W) and Ny-Ålesund (78°55'N, 11°56'E). The location of the stations can

be found in Fig. 1, and radiation data is provided by Cox and Halliwell (2021), Riihimaki et al. (2023) and Maturilli (2020), respectively. The uncertainty standards for the BSRN data is given by McArthur (2005).

3 Results and discussion

3.1 Observed ice-nucleating particle concentrations at Andenes

200 The measured ambient INP concentrations spanned two orders of magnitude at -15°C, and ranged between 10^{-4} and 10^{-1} INP L^{-1} within the temperature range investigated (see Fig. 2). These values are consistent with recent INP observations conducted in Ny-Ålesund (78°55' N, 11°56' E) during autumn 2019 and spring 2020 by Li et al. (2022) and in Nordmela, NO (69°8' N, 15°40' E) located 25 km south of Andenes during the spring of 2020 (Geerts et al., 2022). In Fig. 2, the measurements are shown together with an exponential fit of the data, as well as the corresponding Ny-Ålesund fit from Li et al. (2022) and

205 parameterizations of seasonal INP observations in northern Greenland (Sze et al., 2023). The more remote Greenland site has lower winter INP concentrations than Andenes in spring, while Greenland in summer has slightly larger concentrations of high-temperature INPs. The seasonal Arctic INP cycle has often been related to local biological marine or terrestrial sources (Creamean et al., 2022; Carlsen and David, 2022; Sze et al., 2023; Pereira Freitas et al., 2023) with higher activity in summer. Arctic glacial dust with high ice-nucleating ability has also been shown to play an important role in the lower troposphere

210 during summer months (Tobo et al., 2019; Kawai et al., 2023). It should be noted that our measurements are a snapshot in time, and the seasonal Arctic INP cycle likely contains both lower and higher INP concentrations compared to our measurements throughout the year.

The proximity to year-round sea-ice free ocean at both Andenes and Ny-Ålesund could explain why INP concentrations in early spring are higher there than winter concentrations in Greenland. Following the trajectories of the air parcels reaching

215 the boundary layer at the Andenes site during measurement times (see Fig. A2), we see that they largely pass through either the Greenland Sea or further south in the North Atlantic in the time prior to the INP measurements. The INP concentrations we measure therefore seem to indeed mainly come from air masses travelling over open ocean, both associated with polar air travelling south (so-called cold air outbreaks), and with southerly winds going into the Arctic. While our measurements are not exclusively from air with Arctic origin, measuring INP concentrations in air going into the Arctic is also relevant to Arctic

220 INP concentrations.

When comparing the various Arctic INP parameterizations to the parameterization of Meyers et al. (1992), it is immediately evident that the M92 fit is not representative of the typical INP concentrations in the Arctic (see Fig. 2), as found in earlier work by e.g. Prenni et al. (2007). This is also not expected, as the M92 fit was based on INP measurements in Wyoming (Rogers, 1982) and Manchester (Al-Naimi and Saunders, 1985), far from – and likely not representative of – the Arctic. The M92 fit has

225 almost two orders of magnitude higher INP concentrations than our measurements at the coldest temperatures and four orders of magnitude higher INP concentrations at the warmest temperatures.

We find that the ambient concentration of aerosols $\geq 0.5 \mu$m does not explain the variability of the 50 % FF temperature (Fig. A1d; $R = 0.25; R^2 = 0.06$). This is contrary to previous studies, e.g. by DeMott et al. (2010), but is consistent with
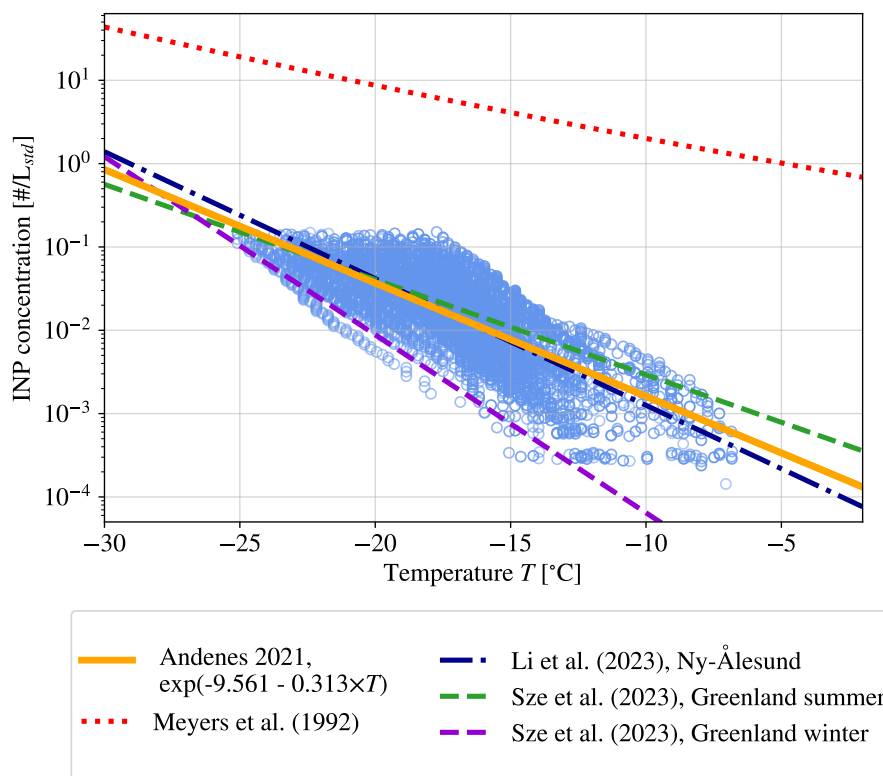
Figure 2. Ice-nucleating particle (INP) concentrations measured from the air at Andenes between 2021-03-15 and 2021-03-30, shown with blue circles. The orange line is the parameterization of INP concentrations as a function of temperature ($R^2 = 0.59$). For comparison, the INP study of Li et al. (2022) from Ny-Ålesund (dark blue), the Greenland summer (green) and winter (purple) study by Sze et al. (2023) is included, as well as the parameterization of Meyers et al. (1992) used in NorESM2.

recent Arctic INP measurements (Li et al., 2022). As noted, total aerosol surface area and INP freezing temperatures show a
230 low correlation as well ($R = 0.28; R^2 = 0.08$), which can be seen in Fig. A1e. This lack of correlation suggests that our INP measurements are dependent on a subset of particles with diameter ≥ 0.5 μm, the minimum cutoff size of our INP collection process, that do not covary with the overall concentration of larger particles.

In the following sections (Sect. 3.2.1 and Sect. 3.3.1), we investigate the impact on cloud phase and radiation from replacing the M92 parameterization in NorESM2 with the observationally-based Andenes 2021 parametrization (hereafter: A21) in the
235 Arctic (latitudes $\geq 66.5°N$). Due to the lack of correlation with aerosol $\geq 0.5\mu$m, we implement the parameterization with temperature dependence only.

3.2 Modelled cloud phase and comparison with supercooled liquid water fractions

3.2.1 Modelled cloud phase

Figure 3 shows the effect of replacing the M92 parameterization with the observationally-based A21 parameterization on ice
cloud fractional occurrence (Fig. 3a), and modelled grid-box averaged ice number concentration (Fig. 3b and 3c). Cold clouds
are defined here as clouds with an ice mixing ratio larger than 10^{-6}. First and foremost, there is a large decrease of around 0.05
in the cold cloud fractional occurrence for the Arctic as a whole, up to heights around 800 hPa (see Fig. 3b). One of the largest
reductions in cold cloud fraction is found at the 859 hPa level, where a local cold cloud maxima in M92 has nearly disappeared
in A21 (see Fig. 3a). This change comes from a decrease in ice crystal number, which can be explored by looking into the grid-
box averaged cloud ice number concentration. The reason we consider grid-box averaged values, that also include averages
over cold cloud free areas, is because the drastic reduction in cold clouds seen in Fig. 3a implies two very different cold cloud
populations between the model experiments, which makes it less straightforward to compare in-cold-cloud quantities between
them. In Fig. 3b, we see a decrease in the cloud ice number of around 200 kg^{-1} at height levels between 900 and 750 hPa. If
we consider annually averaged relative ice number changes at 859 hPa, where we had the largest cold cloud fraction decrease,
we see that there is a large reduction over the Arctic in general, of up to 50 % in some places (see Fig. 3c). There are slightly
stronger reductions over places that are in closer proximity to open ocean and warmer surface temperatures, most prominently
the Bering strait, Baffin Bay and the Norwegian Sea. While perhaps being more susceptible to INP parameterization changes
in the first place, due to warmer temperatures, these areas are generally more cloudy as well, making it easier to notice changes
in the grid-box averaged values. Additionally, we see slight average increases in cloud fraction over Greenland and the sea ice
covered areas, which we do not see over the Norwegian Sea or Baffin Bay (see Fig. B1b). While we expect a longer cloud
lifetime and therefore increased cloud fraction when ice number concentrations decrease, as glaciating processes are reduced,
the decrease in cloud fraction is more difficult to interpret in these idealised conditions where sea surface temperatures are
fixed. Overall, there is a $\sim 2\%$ relative increase in cloud fraction in the Arctic (see Fig.B1d). The largest increases take place
over the sea-ice covered Arctic in boreal autumn and winter, being slightly offset by small negative changes over the Norwegian
Sea.

The changes in cloud fraction in Fig. B1 are quite small, however, compared to the changes we further see in vertically
integrated, absolute cloud phase change. The total grid-box cloud ice water path (CIWP) and cloud liquid water path (CLWP)
change, separated by season, are seen in Fig. 4 and Fig. 5, respectively. Here, the changes are shown in absolute numbers
in order to compare more directly with the absolute changes in cloud radiative effect in Sect. 3.3.1. The relative changes for
selected areas in CIWP (CLWP) can be found in Fig. 6b (Fig. 6d).

The strongest decrease in CIWP happens over the Norwegian Sea in boreal autumn (SON) and winter (DJF), with some
smaller changes in spring (MAM, see Fig. 4). In summer (JJA), the decrease is quite uniform over the whole Arctic, but of a
slightly lower magnitude. For the Arctic in general, the largest decrease in CIWP appears in autumn, as can also be seen from
the blue line in Fig. 6a. The average all-year relative change in the whole Arctic is around -14 %.
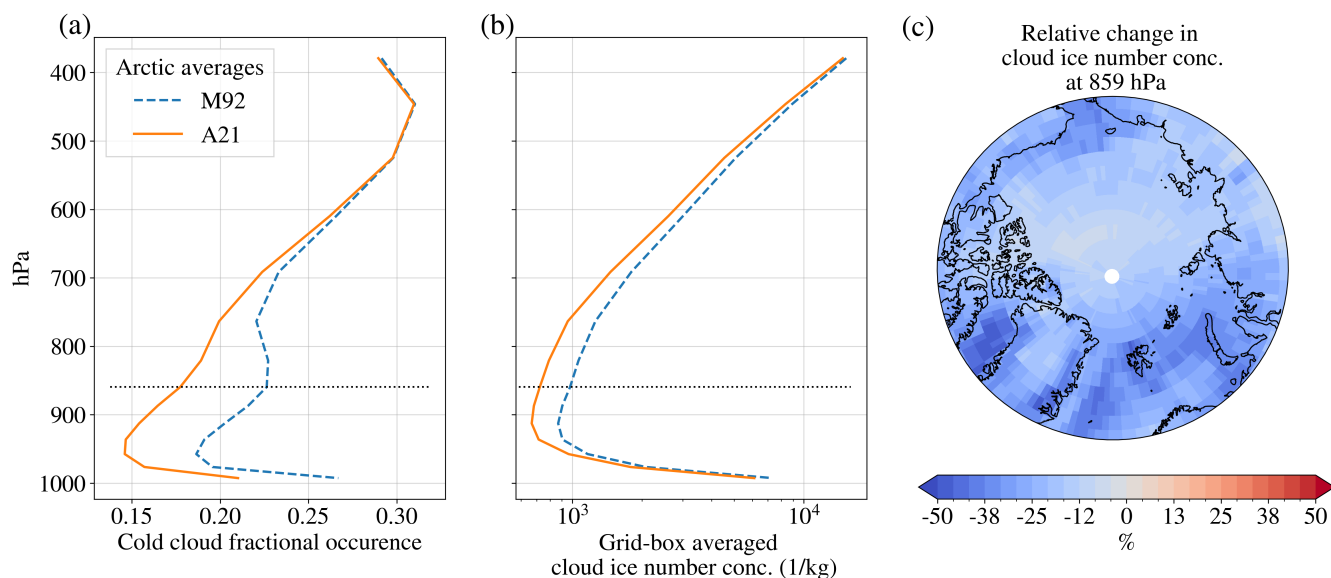
Figure 3. The average ice cloud fractional occurrence (a) and grid-box averaged cloud ice number concentration (b) for M92 and A21, averaged over the period 2007-04-15 to 2010-03-15. The profiles are averages over all latitudes above 66.5°N for height levels in hybrid sigma pressure coordinates (midpoint). The height level is marked with a black dotted line in panel (a) and (b). The relative change in ice cloud fractional occurrence from M92 to A21 at pressure level 859 hPa is shown in (c). Areas with open ocean area ≥ 85 % for more than 50 % of the year are hatched with black dots in (c).

The CLWP changes (see Fig. 5) follow a similar spatial pattern as the CIWP changes, except that a decrease in CIWP corresponds to an increase in CLWP, with a much larger magnitude. For example, the decrease of around 4 gm^{-2} in CIWP that we see over Ny-Ålesund in October in Fig. 6a corresponds to an increase of 40 gm^{-2} in CLWP in Fig. 6c. The average all-year relative increase in CLWP over the Arctic is around 65 %.

This large difference in magnitude between CIWP and CLWP changes could be explained by the Wegener–Bergeron–Findeisen (WBF) process (Wegener, 1911; Bergeron, 1928; Findeisen, 1938; Storelvmo and Tan, 2015). The rapid growth of ice crystals can cause the clouds to dissipate faster, as the particles reach large enough sizes to fall out from the cloud at a quicker rate than through the growth of liquid particles. A significant reduction in ice particles can contribute to a reduction in the efficiency of the WBF process, and thereby lead to a liquid water content in the clouds much higher than the reduction in ice content itself, as the liquid water is no longer changing phase and precipitating out of the cloud at the same rate. Interestingly, we see that while the relative change in CIWP was largest over Ny-Ålesund in Fig. 6a, the largest relative changes in CLWP are over Alert and the North Pole, where we see extremely large relative changes, reaching over a 1000 % change or more in some seasons. These are places with very low CLWP in M92, causing the change in CLWP in A21 to make a relatively larger impact than over Ny-Ålesund, even though the absolute change is much higher here.
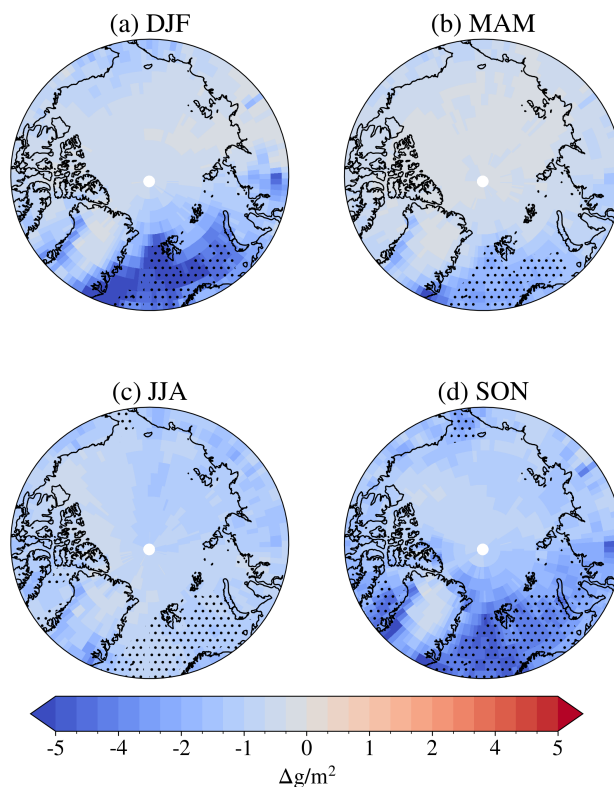
Figure 4. Differences in total grid-box cloud ice water path between A21 and M92 by season (averaged by season over the period 2007-04-15 to 2010-03-15). Negative values correspond to lower cloud ice water path in A21 compared to M92. Areas with open ocean area $\geq 85\%$ for more than 50 % of the season are hatched with black dots.

3.2.2 Comparison to observed supercooled liquid water fractions

285   In order to see how the changes in modelled cloud phase due to the parameterization adjustment compares to actual observations, a comparison between the SLW fraction for each cloud isotherm in the model and in CALIPSO lidar observations is included in Fig. 7.

In order to see how the changes in modelled cloud phase due to the parameterization adjustment compares to actual observations, a comparison between the SLW fraction for each cloud isotherm in the model and in CALIPSO lidar observations is included in Fig. 7.

For the bulk of the cloud (dashed lines), the A21 parameterization adjustment produces SLW fractions much closer to the observations than M92. M92 shows around 20 % lower SLW fraction for temperatures between -25°C and -10°C. A21
290   reduces this gap to around 5 % less SLW fraction compared to observations, with virtually all A21 SLW fraction values falling within one standard deviation of the lidar measurements. For cloud top, the A21 experiment overestimates the SLW fractions, especially for temperatures less than -15°C. At colder temperatures of -25°C and -30°C, M92 and A21 diverge drastically for cloud top, with a difference in SLW fraction as large as 60 %. While it is clearly seen that the unrealistically high Arctic INP concentration in M92 causes excessive ice formation, it is less clear why A21 performs well for the bulk of the cloud, while
295   overestimating somewhat the cloud top SLW fraction. The fact that secondary ice production is limited to 1000 m^{-3}s^1 is not
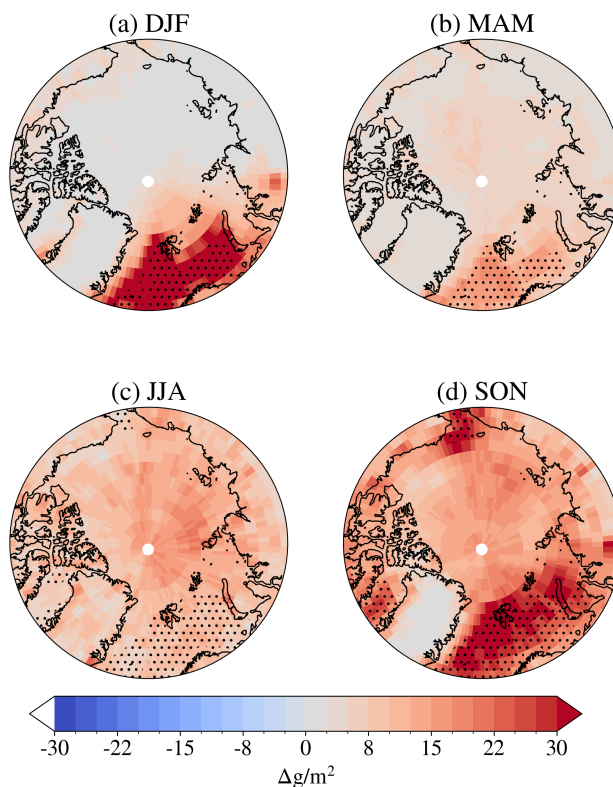
Figure 5. Differences in total grid-box cloud liquid water path between A21 and M92 by season (averaged by season over the period 2007-04-15 to 2010-03-15). Positive values correspond to a higher cloud liquid water path in A21 compared to M92. Note that the colorbar extends to sixfold the extent of the colorbar in Fig. 4. Areas with open ocean area $\geq 85\%$ for more than 50 % of the season is hatched with black dots.

likely to play a role in overestimating SLW, as the parameterization is only active at temperatures between -8°C and -3°C. At these temperatures, the cloud top SLW fraction in both model experiments and observations is close to 100 %. However, the fact that our model setup hinders ice detrainment at mixed-phase temperatures could perhaps be cutting off a relevant source of cloud top ice, which is not as apparent in M92 due to the already excessive ice production. Another possible explanation could simply be that simulated ice crystals sediment at too high a rate from the cloud top to the interior of the cloud. Overall, A21 improves the SLW fractions in Arctic clouds, performing best for bulk cloud and coming closer to observations at cloud top, despite the overestimation in cloud top SLW fraction at cold temperatures below ∼ -25°C.

300
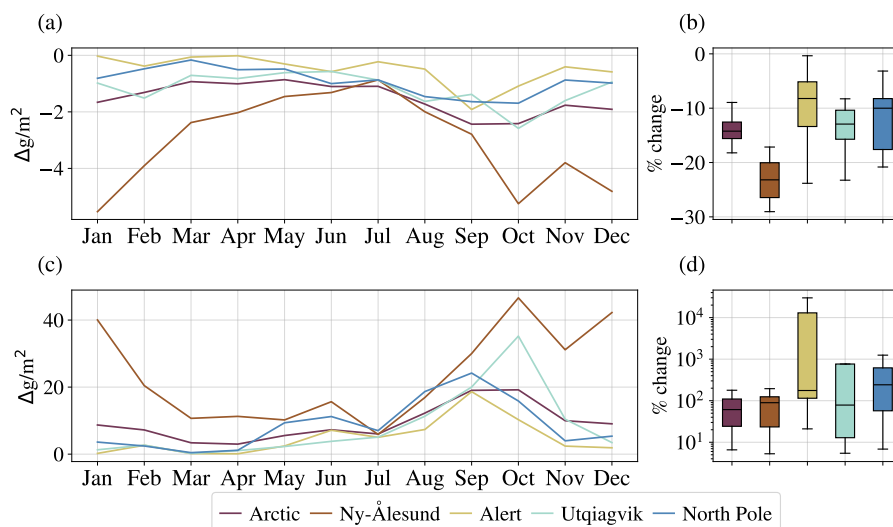
Figure 6. The change in total grid-box cloud ice water path (a-b) and liquid water path (c-d) between A21 and M92, averaged over the period 2007-04-15 to 2010-03-15. Left: absolute change for each month averaged over selected regions. Right: the distribution of relative change over the months in the same regions.

3.3 Modelled cloud radiative effects and comparison with observed radiative fluxes

3.3.1 Modelled cloud radiative effects

305 The differences in shortwave cloud radiative effect at the surface between A21 and M92 across the Arctic, divided by season, can be seen in Fig. 8. The calculation of cloud radiative effect at the surface can be found in Sect. B2. As expected, the change is highly dependent on the solar zenith angle, giving large absolute values during the sun-rich summer and late spring months, and close to zero changes for the winter months and at latitudes above 80°N in autumn. In summer, the change ranges from 2 to 8 Wm^{-2} less incoming solar radiation in A21 over the entire Arctic, consistent with the pattern of CLWP change in summer

310 seen in Fig. 5. The average change across the Arctic is around -3 Wm^{-2} in summer, which can be seen from Fig. 10a. In spring, the largest change is located over the Norwegian Sea, with values between -5 and -8 Wm^{-2}. This is also the region where we find the largest increase in spring CLWP. In autumn, the change is around -1 to -2 Wm^{-2} at latitudes below 80° and Greenland, where the change is close to zero. This corresponds well with the distribution of CLWP change as well, taking into account that there is much less solar radiation in autumn than in spring and summer and a significantly lower increase in

315 CLWP over Greenland in autumn compared to the rest of the Arctic in A21. These changes culminate in an average relative change in surface shortwave cloud radiative effect across the Arctic of around -15 % (Fig. 10a).

The seasonal change in surface longwave cloud radiative effect between A21 and M92 across the Arctic is seen in Fig. 9.

The increase in the longwave cloud radiative effect due to increased CLWP is non-linear. The longwave cloud radiative effect is dependent on the cloud's longwave emissivity, which can be highly sensitive to changes in CLWP if it increases from
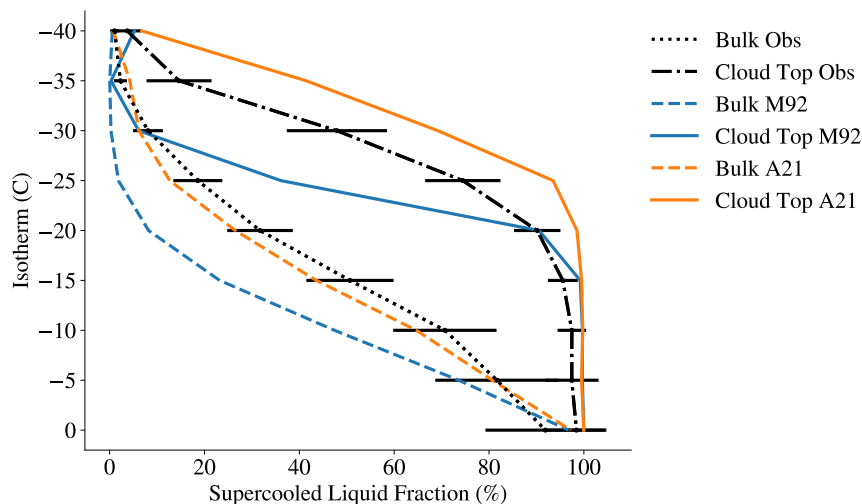
Figure 7. The supercooled liquid water (SLW) fraction for each isotherm in clouds for latitudes above 66.6°N and below 82°N. The dashed lines show the fraction for bulk cloud in the modelled climate, and the solid lines show the fraction for cloud top (CT) in the modelled climate, both in M92 (blue) and A21 (orange), averaged over the period 2007-04-15 to 2010-03-15. The black dotted line shows the SLW fraction for the bulk cloud as observed by the CALIOP lidar, while the dashdotted line shows the same for cloud top, averaged over the period 2009-06-01 to 2013-05-31. The error bars correspond to one standard deviation in the lidar measurements.

320 previously small values, but is insensitive if the previous value was large. This is in contrast to the shortwave cloud radiative effect, for which the relationship with CLWP is closer to linearity. Taking the longwave emissivity dependence into account, the changes in longwave cloud radiative effect at the surface can largely be explained by the changes in CLWP as well. A rough estimation of the cloud longwave emissivity change, divided by season, can be found in Fig. B2, with a description of the calculation in Sect. B3.

325 In the winter months, the largest increases in longwave cloud radiative effect can be found along the ice edge west, north and east of Svalbard, with values approaching 10 to 15 Wm^{-2}. The increase in this area is even more pronounced than the changes we might expect in cloud longwave emissivity (see Fig. B2), compared to the rest of the Arctic. This is likely due to the fact that this area is cloudier than the rest of the Arctic, making it more affected by the emissivity changes. In spring, the increase in longwave cloud radiative effect is strongest north and east of Svalbard, which is also where we see the strongest changes in

330 cloud longwave emissivity. It is interesting to note that we observe little change in the longwave cloud radiative effect over the Norwegian Sea, even though the change in shortwave cloud radiative effect is between -5 and -8 Wm^{-2} in spring. This can be explained by the clouds in this area already containing a fair amount of liquid water, so the resulting change in CLWP makes little difference to the cloud longwave emissivity (Fig. B2), while still having an effect on the cloud's reflection of shortwave radiation. In summer, what stands out is the comparatively large increase of longwave cloud radiative effect, between 5 and

335 10 Wm^{-2}, over Greenland. This corresponds to a large increase in cloud longwave emissivity, which is absent for the rest of
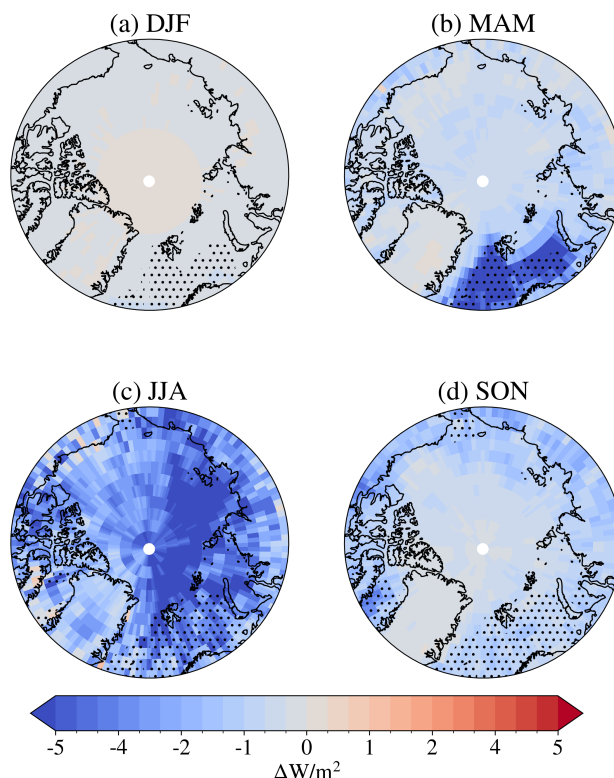
Figure 8. Differences in shortwave cloud radiative effect at the surface between A21 and M92 by season (averaged over the period 2007-04-15 to 2010-03-15). Negative values correspond to more solar radiation being reflected by the clouds in A21 compared to M92. Areas with open ocean area $\geq 85\%$ for more than 50 % of the year are hatched with black dots.

the Arctic. The small increases in longwave cloud radiative effect we see over the sea ice covered Arctic might result from the general increase in low-level clouds (Fig. B1). In autumn, the increase is large (between 5 and 10 Wm^{-2}) over the entire Arctic, except for over the Norwegian Sea and parts of Greenland, where the CLWP increase is low (Fig. 5).

The total relative change in longwave cloud radiative effect across the Arctic is around 15 %, as seen in Fig. 10d. In
340   Ny-Ålesund, the changes are largest in winter, while Alert and the North Pole, as well as the Arctic in general, show the largest changes in autumn, as well as a minor peak in spring. While the magnitude of change is comparable in Ny-Ålesund, approaching 15 Wm^{-2} increased longwave cloud radiative effect in December, the average relative changes are largest over Alert and the North Pole.

3.3.2   Comparison with observed radiative fluxes

345   As the changes we see in surface longwave cloud radiative effect are quite drastic, it is natural to wonder whether the new state in A21 actually corresponds to a plausible climate. The cloud effect on outgoing longwave radiation at the TOA is negative, and
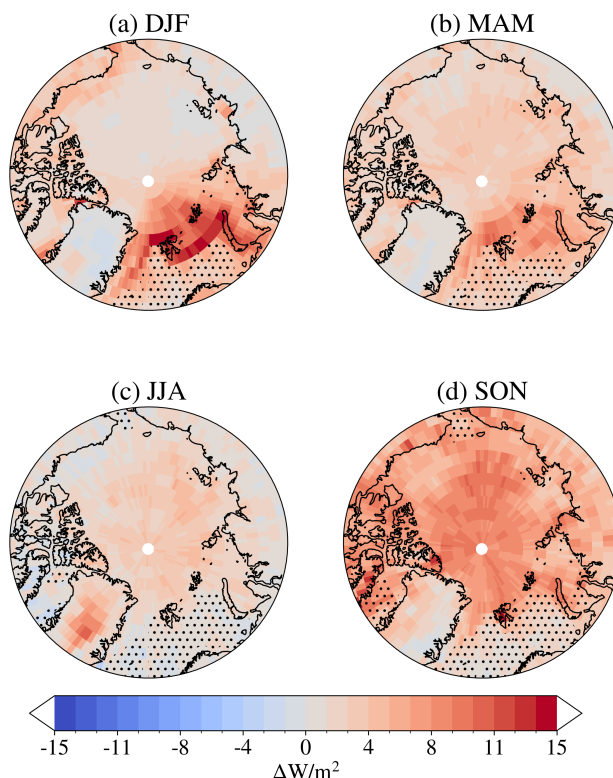
Figure 9. Differences in longwave cloud radiative effect at the surface between A21 and M92 by season (averaged by season over the period 2007-04-15 to 2010-03-15). Positive values correspond to more downwelling longwave radiation from clouds to the surface in A21 compared to M92. Note that the colorbar extends to threefold the extent of the colorbar in Fig. 8. Areas with open ocean area $\geq 85\%$ for more than 50 % of the season are hatched with black dots.

most so during late summer and autumn. In Fig. 11, we see the estimated cloud effect on outgoing longwave TOA flux from satellite measurements. First and foremost, we see that both M92 and A21 fall within the uncertainty estimates of CERES, indicating that as far as available measurements are concerned, the model representations fall within what we consider realistic

350 values of radiation fluxes. While the difference between M92 and A21 at TOA is smaller than at the surface, A21 predicts a more negative cloud effect on outgoing longwave flux, as expected. This is especially clear in September and October each year, when the largest change in CLWP takes place. While the largest change in cloud longwave emissivity is estimated to be in winter and autumn (see Fig. B2), the autumn likely shows larger longwave cloud radiative effect changes due to the combination of high emissivity change and a larger amount of outgoing longwave radiation to intersect.

355 In Fig. 12, we consider the radiation fluxes at the surface level instead of revisiting the Arctic areas we have examined earlier. The measurements are point-observations, without a possibility to isolate cloud radiative effects, and the corresponding model grid-boxes are quite large and cover varied surfaces. We therefore investigate the net radiation flux at the surface in order to compare the model experiments and radiation measurements more easily. Our focus is, however, first and foremost
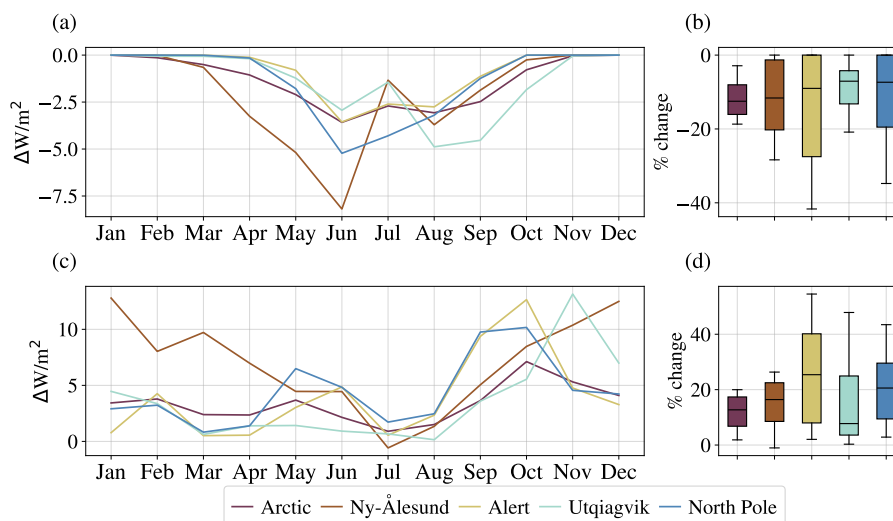
Figure 10. The change in total grid-box shortwave (a-b) and longwave (c-d) cloud radiative effect between A21 and M92, averaged over the period 2007-04-15 to 2010-03-15. Left: absolute change for each month averaged over selected regions. Right: the distribution of relative change over the months in the same regions.
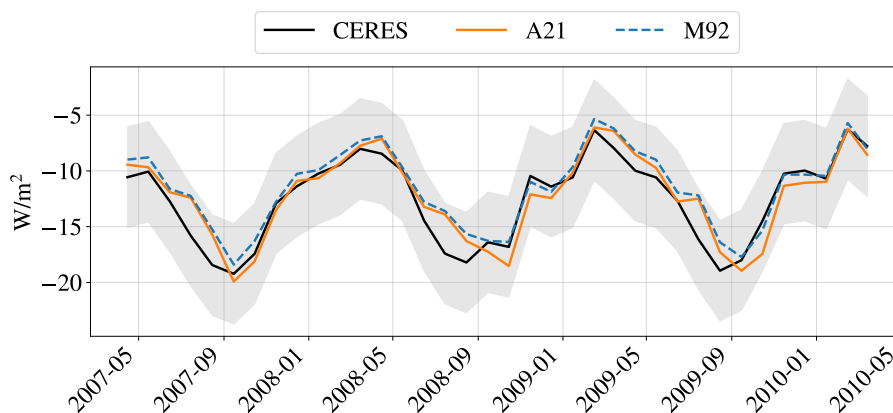
Figure 11. Cloud radiative effect on outgoing longwave radiation at the top of the atmosphere, as estimated by CERES (black line) and modelled by NorESM in M92 (blue line) and A21 (orange line). Gray shaded area corresponds to the CERES instrument uncertainty.

on longwave fluxes in winter and autumn, when the shortwave fluxes play less of a role. For all the stations, we see that the
360 magnitude of the negative net surface flux in winter is overestimated by the model simulations, pointing to a negative net radiation bias in the model in winter. However, this bias is smaller in A21 than M92. The biggest differences between the model experiments occur in Ny-Ålesund, where changes in cloud radiative effect clearly bring A21 more in line with observed winter-time flux. From this, we can draw the conclusion that the cloud radiative effect simulated in A21 brings NorESM2
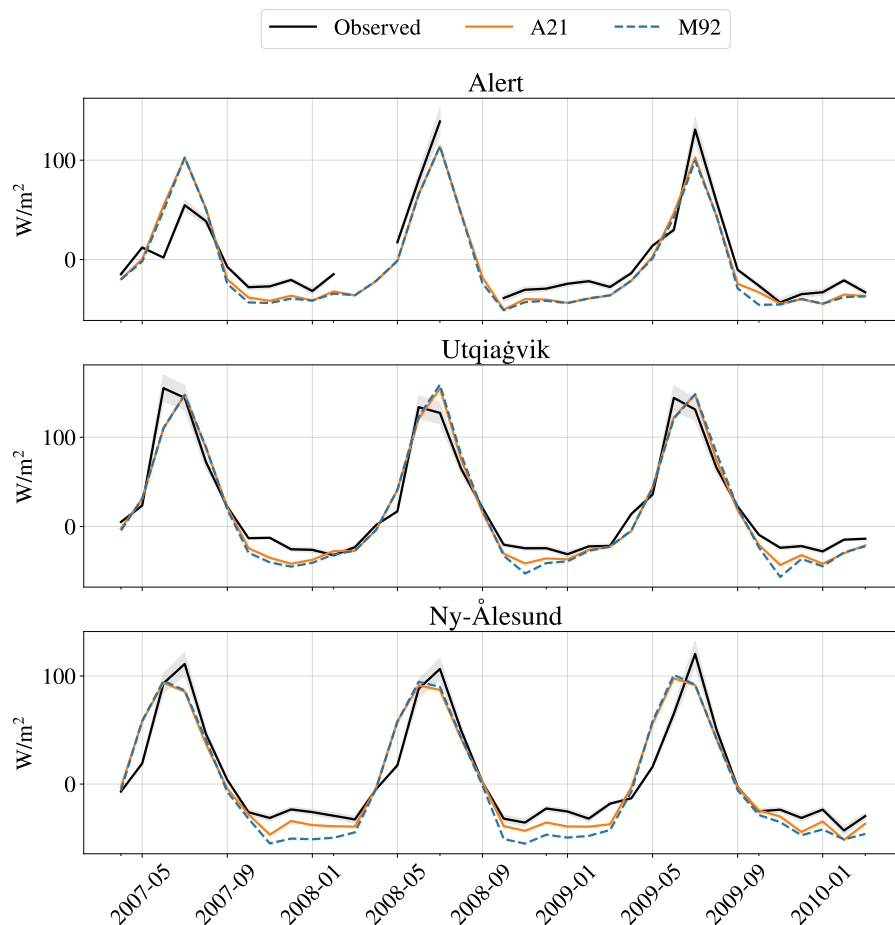
Figure 12. Net surface flux at various stations, from BSRN point-observations on the ground (black line) and corresponding grid-box values modelled by NorESM2 in M92 (blue line) and A21 (orange line). Gray shaded area corresponds to the instrument uncertainty standards.

closer to realistic radiation flux values, albeit without compensating completely for radiation biases. It is interesting to note that the new parameterization reduces the gap between observed and modelled radiative fluxes the most in Ny-Ålesund, where we also expect our INP measurements to be most representative due to their similarity with Li et al. (2022).

To give an indication of the implications of these changes in cloud radiative effects, the changes in surface temperature between M92 and A21 across the Arctic domain are included in Fig. 13c, together with the net cloud radiative effect change throughout the year in Fig. 13a. It should be stressed that the surface temperature changes shown here are not representative of the full response to the radiation changes, as the sea surface temperatures are fixed in the model, and also, the temperature changes over land and sea ice will be muted due to the fixed sea surface temperatures. For the Arctic in general (the blue line in Fig. 13c), we can see an average annual increase in A21 compared to M92 of $0.3°C$, with a maximum in October of $0.7°C$. This corresponds to an October net surface flux increase of 6 Wm^{-2}. The largest temperature changes are found over
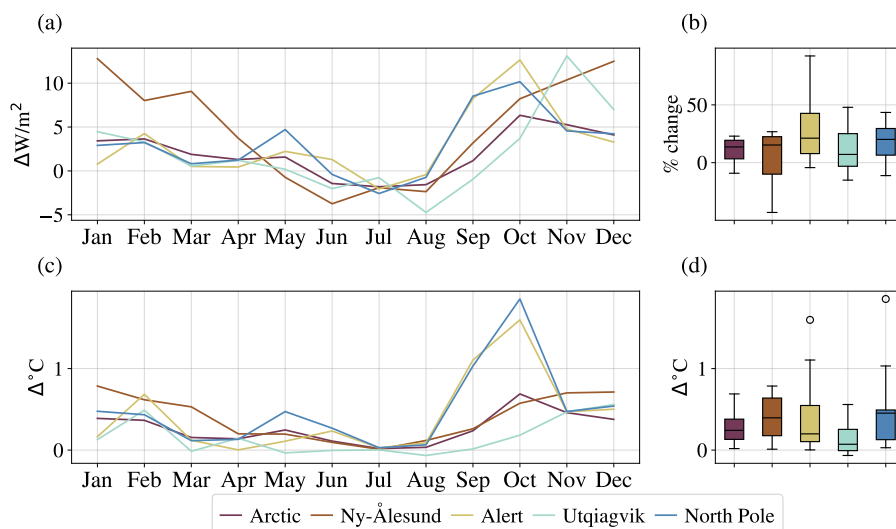
Figure 13. The change in net cloud radiative effect (a-b) and surface air temperature (c-d) between A21 and M92, averaged over the period 2007-04-15 to 2010-03-15. Left: absolute change for each month averaged over selected regions. Right: the distribution of relative change over the months in the same regions.

the North Pole and Alert, of between $1.5°C$ and $2°C$. Ny-Ålesund and Utqiagvik show similar increases as the former areas in

375   the magnitude of net surface flux, but due to the closer proximity to open ocean with fixed temperature, these areas likely show a more muted response in these simulations. This likely also explains why the North Pole shows a slightly larger temperature response than Alert. To determine the full temperature response of such a parameterization change, model experiments with dynamic oceans are necessary. These results, however, show that using observationally constrained INP concentrations has a large impact on the simulation of Arctic surface climate, and that using more realistic concentrations can be an important step

380   in improving model simulations.

4 Conclusions

In this study, we have found that Arctic clouds and their radiative effect are indeed sensitive to the INP parameterization, as shown in previous work by e.g. Xie et al. (2013). In attempting to constrain INP concentrations in the NorESM2 model using Arctic observations, we have quantified INPs active in the immersion freezing mode in Andenes in March 2021. Contrary to

385   DeMott et al. (2010), but in line with previous Arctic measurements (Li et al., 2022; Sze et al., 2023), we observed negligible correlations between INP freezing temperatures and the presence of ambient aerosols with diameter ≥ 0.5 μm. Indeed, temperature was the best indicator of INP concentrations that we could find, underscoring perhaps that the Arctic INP populations differ in composition from those at lower latitudes in a way that makes them more difficult to capture with general INP schemes. The parameterization of the concentration as a function of temperature (A21) deviates two to four orders of

magnitude from the Meyers et al. (1992) (M92) parameterization, designed for lower latitudes, but shows close similarity to the measurements of Li et al. (2022), taken at Ny-Ålesund in Fall 2019 and Spring 2020. From comparison with measurements in northern Greenland, however, we see that our measured concentrations are higher than the Greenlandic winter average, but slightly lower than the summer average (Sze et al., 2023). This could be an indication that our measured concentrations are on the higher end of what we would expect in winter in the rest of the Arctic, further from open ocean, but this remains to be investigated.

The implementation of an observation-based INP parameterization for the Arctic in NorESM2 was shown to make a substantial impact on the ice and liquid content of low-level Arctic clouds. The total grid-box CIWP was reduced by 15 % over the entire Arctic, the absolute changes being largest in boreal autumn, followed by winter. The total grid-box CLWP correspondingly increased by 65 % over the entire Arctic, with absolute changes in autumn of around 20 gm^{-2}. This led to a significant improvement in modelled SLW fractions for each cloud isotherm compared to spaceborne lidar observations using CALIOP.

The same implementation led to increases in longwave cloud radiative effect at the surface in autumn, winter, and spring due to increased cloud optical thickness that dominated the decrease in shortwave cloud radiative effect at the surface in summer. The result led to an average increase in net cloud radiative effect at the surface of 2 Wm^{-2} over the entire Arctic, with more than a 5 Wm^{-2} increase in October and November. While these changes are quite drastic, they do not appear to make the simulated radiative fluxes less consistent with observations. The changes in the cloud radiative effect showed an overall increase in average annual surface temperature of 0.3°C, with a maximum of 0.7°C in October, but which can only be considered a lower limit of a possible temperature effect as the sea surface temperatures are fixed in the model simulation. The large increase in surface longwave radiative effect compared to shortwave is likely due to the non-linear relationship between cloud longwave emissivity and CLWP, causing the longwave emissivity to increase drastically as the CLWP increased from low values in autumn, winter and spring. The same non-linear relationship could matter for the role of cloud phase in future Arctic climate. With warming, we expect to see CLWP increases in Arctic clouds, and perhaps increased cloud radiative effect at the surface as the clouds become optically thicker. Exactly how warming will affect the cloud radiative effects, however, is not given. If we imagine a warming Arctic starting from a cloud ice content similar to M92, the non-linearity of longwave emissivity could perhaps create a larger increase in longwave cloud radiative effect than if we start from conditions similar to A21, as found by Tan and Storelvmo (2019). How such effects will be, however, is the outcome of a delicate interplay between cloud microphysical processes and climate change, about which there are still multiple uncertainties.

While this study supports that more realistic and regionally tailored INP parameterizations in climate models could be an important step for improved climate simulations, it also makes evident the pressing question of what role INPs will play in the future. Answering this question requires INP parameterizations that are not only latitude-dependent functions of temperature, such as ours, but the ones that are responsive to changes in relevant environmental factors based on physically established relationships. They need to be able to represent seasonal and spatial variations as well as warming-induced changes to the environment. Predicting the future effect of INPs also depends on being able to represent other relevant cloud microphysical processes, such as secondary ice production, in a satisfactory way. These will be important steps towards a better understanding

of the role cold clouds play in Arctic and global warming and limiting the uncertainty in climate predictions (Prenni et al., 2007;
425   Murray et al., 2021).

Code and data availability.   The data sets produced for this study, both INP measurements and modelling results, can be found at https:
//doi.org/10.5281/zenodo.11617774. The CALIOP L2 data used to derive SLF metrics and the CERES EBAF data can be downloaded freely
at https://search.earthdata.nasa.gov/. The surface radiation flux can be downloaded freely at https://www.pangaea.de/. The ERA5 data used to
produce the back trajectories can be found at https://doi.org/10.24381/cds.bd0915c6. The surface air pressure observations in Andenes can be
430   downloaded from https://thredds.met.no/thredds/catalog/met.no/observations/surface/87110/178/catalog.html. The colormap from Crameri
et al. (2020) was used when preparing the figures.

Appendix A: Ice-nucleating particle observations

A1   Aerosol measurements

The relationships between INP freezing temperatures and ambient aerosols with diameter $\geq 0.5\mu$m is shown in Fig. A1.

435 ### A2   Air parcel back trajectories

The potential source regions of INPs were identified from an analysis based on kinematic backward trajectories computed
with LAGRANTO (Sprenger and Wernli, 2015). Using 3-hourly ERA5 reanalysis fields (Hersbach et al., 2023), air parcels
were traced backwards from the location of Andenes for 10 days. Potential INP source locations where then extracted from
the backward trajectories by finding locations where air masses arriving at low levels over Andenes were in potential contact
440   with the surface during the last 3 days before arrival. To this end, trajectory points were identified by (i) selecting air parcel
trajectories that were arriving with a pressure difference of less than 20 hPa to the surface pressure (corresponding to a height
of ~500 m above ground) at Andenes at the time of arrival, and (ii) along these trajectories, extracting the locations during the
last 72 h before arrival where the air parcel was within 20 hPa of the surface pressure. Trajectories were only considered for
those 3 h time windows where an INP sample had been taken. A map of these locations shows a concentration of potential INP
445   source locations in the vicinity of the measurement site. Most locations are within the Norwegian Sea, with some branches
going towards Greenland Sea and Fram strait, the Iceland Sea, and towards the North Atlantic (Fig. A2).

Appendix B: Modelled cloud and radiation properties

B1   Cloud cover

The modelled cloud fraction changes are shown in Fig. B1.
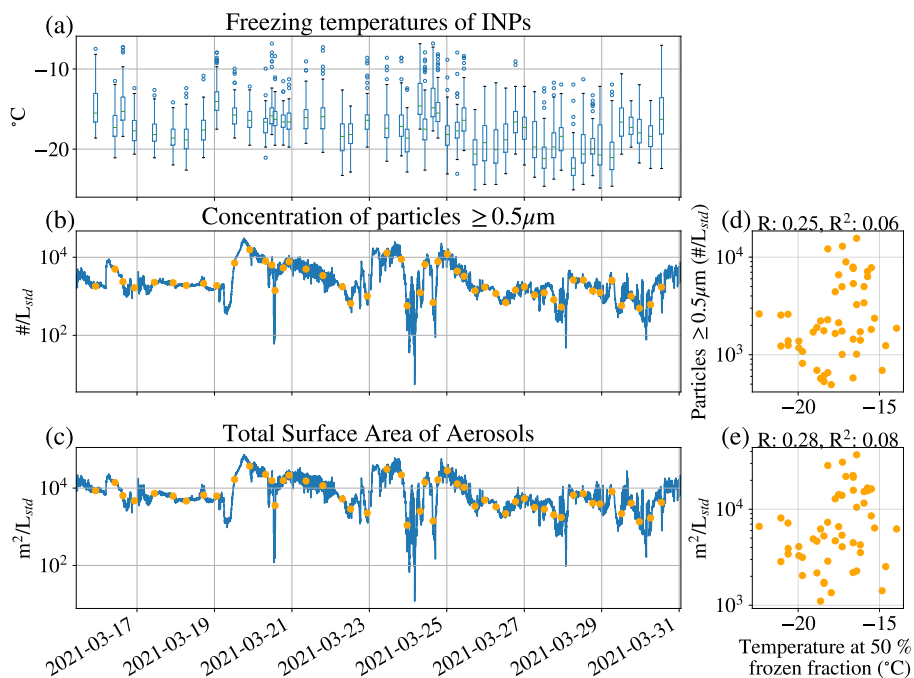
Figure A1. Freezing temperatures of all INP measurements in Andenes 2021 (a), compared with simultaneous measurements of ambient aerosols with diameter $\geq 0.5\mu$m (b) and with total aerosol surface aera (c). The orange dots in (b) show the average values over the INP sampling period, which are used for relationship estimation between the temperature at 50 % frozen fraction with larger aerosols in (d) and total aerosol surface aera in (e).

B2 Calculation of cloud radiative effect

The modelled cloud radiative effect (CRE) at the surface for shortwave (SW) and longwave (LW) radiation is calculated as

$$SW_{CRE,surface} = SW_{net,surface} - SW_{net,clearsky,surface} \tag{B1}$$

$$LW_{CRE,surface} = LW_{net,surface} - LW_{net,clearsky,surface}, \tag{B2}$$

where downwelling radiation is defined as positive for both quantities. The modelled cloud radiative effect (CRE) at TOA for longwave (LW) radiation is calculated as

$$LW_{CRE,TOA} = LW_{out,TOA} - LW_{out,clearsky,TOA} \tag{B3}$$

where upwelling radiation at TOA is defined as positive.
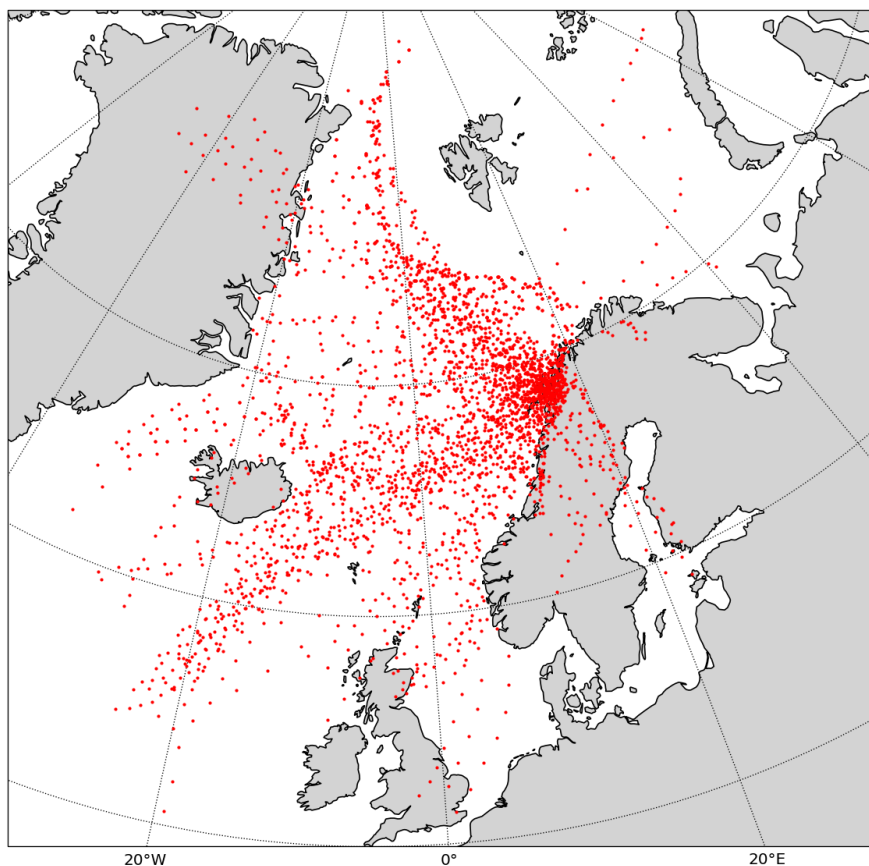
Figure A2. Air parcel back trajectory locations for 72 hours prior to INP measurements times, shown for when the air parcel was within 20 hPa of the surface pressure, or approximately 500 m height above ground. The trajectories are restricted to those arriving within 20 hPa from the surface pressure.

B3   Cloud longwave emissivity

To get a rough estimate of the downward cloud longwave emissivity (CLWE) we can expect from the simulated cloud liquid
460   water path (CLWP), we calculate the CLWE based on the total grid-box CLWP as

$$\mathrm{CLWE} = 1 - \exp(-k \times \mathrm{CLWP}), \tag{B4}$$

where k is the mass absorption coefficient. We use $k = 0.158$ m^2/g, the standard US value found by Stephens (1978). It should
be noted, however, that this value may vary slightly from place to place. The estimated CLWE changes can be found in figure
B2.
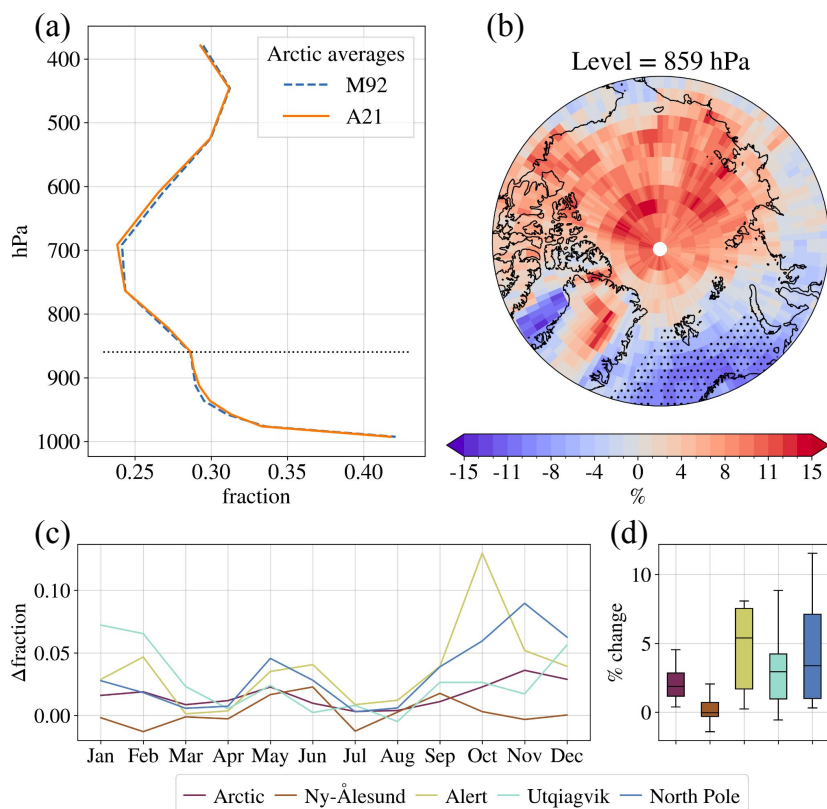
Figure B1. The cloud fraction for the M92 and A21 model experiments, averaged over the period 2007-04-15 to 2010-03-15. (a): the average values over all latitudes above 66.5°N for height levels in hybrid sigma pressure coordinates (midpoint). (b): the relative change from M92 to A21 at pressure level 859 hPa. The level is marked with a black dotted line in the left plot. (c) shows the total vertically-integrated cloud fraction. Left: absolute change for each month averaged over selected regions. (d): the distribution of relative change over the months in the same regions.

465 *Author contributions.* Authors ABG, ROD, TC and FH all participated in performing INP measurements. Authors ROD, TC, FH and TS planned and implemented the measurement campaign, and outlined the measurement strategy, together with HS. ABG ran all model simulations, with assistance and contributions from TS, SH and ZM. SH and ZM provided model code modification. ABG, SH and HS produced the figures. ABG wrote the manuscript, together with TS and ROD. All authors reviewed and commented on the manuscript.

Competing interests. We declare that we have no competing interests.
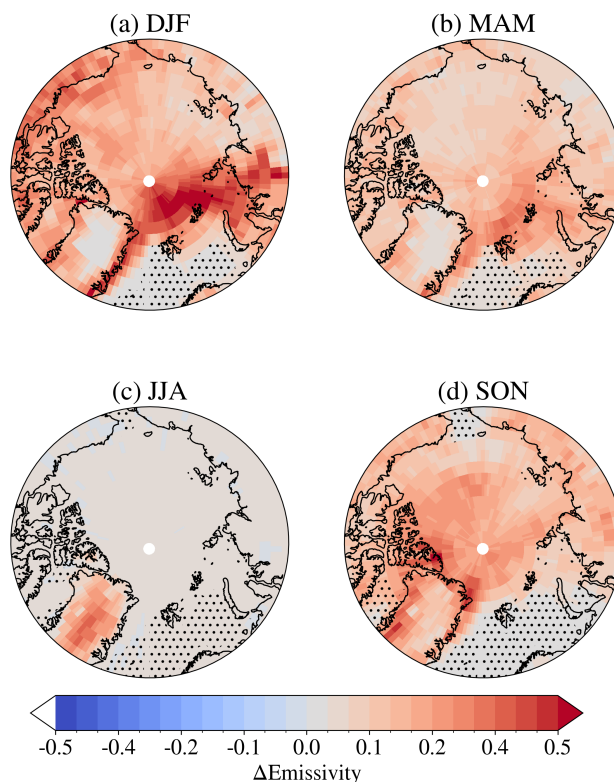
Figure B2. Differences in estimated cloud longwave emissivity between A21 and M92 by season (averaged by season over the period 2007-04-15 to 2010-03-15). Positive values correspond to higher longwave emissivity of clouds in A21 compared to M92.

470 *Acknowledgements.* This work was supported by the European Research Council (ERC) through Grant StG 758005, as well as Grant CoG 101045273. ROD would also like to acknowledge support from EEARO-NO-2019-0423/IceSafari, contract no. 31/2020 under NO Grants 2014–2021 (EEA Grants/ Norway Grants) and the EU-HORIZON-WIDERA-2021 Grant no. 101079385. HS acknowledges support from the European Commission within the Horizon 2020 programme (Grant no. 773245). Resources for simulations and data storage were provided by UNINETT Sigma2, the National Infrastructure for High Performance Computing and Data Storage in Norway. We acknowledge all those

475 involved in the joint measurement campaign between MC2 and ISLAS. This includes Alena Dekhtyareva, Aina Marie Johannessen, Britta Schäfer, Andrew Seidl and Iris Thurnherr, in addition to the aforementioned authors. Iris Thurnherr is especially acknowledged for her role in calculating air parcel trajectories during the field campaign. The campaign was facilitated by Andøya Space. We would also like to thank Dr. Jörg Wieder and Dr. Michael Rösch from ETH-Zürich for providing key equipment for the aerosol measurement setup. Finally, we would like to thank the University of Oslo, Department of Geosciences Cold Climate Container (C3) infrastructure for providing the lab facilities

480 for DRINCO.

References

Al-Naimi, R. and Saunders, C.: Measurements of natural deposition and condensation-freezing ice nuclei with a continuous flow chamber, Atmospheric Environment (1967), 19, 1871–1882, https://doi.org/https://doi.org/10.1016/0004-6981(85)90012-5, 1985.

Ansmann, A., Tesche, M., Althausen, D., Müller, D., Seifert, P., Freudenthaler, V., Heese, B., Wiegner, M., Pisani, G., Knippertz, P., and Dubovik, O.: Influence of Saharan dust on cloud glaciation in southern Morocco during the Saharan Mineral Dust Experiment, Journal of Geophysical Research: Atmospheres, 113, https://doi.org/https://doi.org/10.1029/2007JD008785, 2008.

Bentsen, M., Bethke, I., Debernard, J. B., Iversen, T., Kirkevåg, A., Seland, Ø., Drange, H., Roelandt, C., Seierstad, I. A., Hoose, C., and Kristjánsson, J. E.: The Norwegian Earth System Model, NorESM1-M – Part 1: Description and basic evaluation of the physical climate, Geoscientific Model Development, 6, 687–720, https://doi.org/10.5194/gmd-6-687-2013, 2013.

Bergeron, T.: Über die dreidimensional verknupfende Wetteranalyse I, Geofys. Publ., 5, 111, 1928.

Bigg, E. K.: The formation of atmospheric ice crystals by the freezing of droplets, Quarterly Journal of the Royal Meteorological Society, 79, 510–519, https://doi.org/https://doi.org/10.1002/qj.49707934207, 1953.

Boer, G., Morrison, H., Shupe, M., and Hildner, R.: Evidence of liquid dependent ice nucleation in high-latitude stratiform clouds from surface remote sensors, Geophysical Research Letters, 38, https://doi.org/10.1029/2010GL046016, 2011.

Bruno, O., Hoose, C., Storelvmo, T., Coopman, Q., and Stengel, M.: Exploring the Cloud Top Phase Partitioning in Different Cloud Types Using Active and Passive Satellite Sensors, Geophysical Research Letters, 48, https://doi.org/10.1029/2020GL089863, 2021.

Carlsen, T. and David, R. O.: Spaceborne evidence that ice-nucleating particles influence cloud phase, Earth and Space Science Open Archive, p. 17, https://doi.org/10.1002/essoar.10510292.1, 2022.

Ceppi, P., Hartmann, D. L., and Webb, M. J.: Mechanisms of the Negative Shortwave Cloud Feedback in Middle to High Latitudes, Journal of Climate, 29, 139 – 157, https://doi.org/10.1175/JCLI-D-15-0327.1, 2016.

Cox, C. J. and Halliwell, D.: Basic measurements of radiation at station Alert (2004-08 - 2014-06), https://doi.org/10.1594/PANGAEA.932867, 2021.

Crameri, F., Shephard, G. E., and Heron, P. J.: The misuse of colour in science communication, Nature Communications, 11, 5444, https://doi.org/10.1038/s41467-020-19160-7, 2020.

Creamean, J. M., Cross, J. N., Pickart, R., McRaven, L., Lin, P., Pacini, A., Hanlon, R., Schmale, D. G., Ceniceros, J., Aydell, T., Colombi, N., Bolger, E., and DeMott, P. J.: Ice Nucleating Particles Carried From Below a Phytoplankton Bloom to the Arctic Atmosphere, Geophysical Research Letters, 46, 8572–8581, https://doi.org/https://doi.org/10.1029/2019GL083039, 2019.

Creamean, J. M., Barry, K., Hill, T. C. J., Hume, C., DeMott, P. J., Shupe, M. D., Dahlke, S., Willmes, S., Schmale, J., Beck, I., Hoppe, C. J. M., Fong, A., Chamberlain, E., Bowman, J., Scharien, R., and Persson, O.: Annual cycle observations of aerosols capable of ice formation in central Arctic clouds, Nature Communications, 13, 3537, https://doi.org/10.1038/s41467-022-31182-x, 2022.

Danabasoglu, G., Lamarque, J.-F., Bacmeister, J., Bailey, D. A., DuVivier, A. K., Edwards, J., and et al.: The Community Earth System Model Version 2 (CESM2), Journal of Advances in Modeling Earth Systems, 12, e2019MS001916, 2209–2221, https://doi.org/https://doi.org/10.1029/2019MS001916, 2020.

David, R. O., Cascajo-Castresana, M., Brennan, K. P., Rösch, M., Els, N., Werz, J., Weichlinger, V., Boynton, L. S., Bogler, S., Borduas-Dedekind, N., Marcolli, C., and Kanji, Z. A.: Development of the DRoplet Ice Nuclei Counter Zurich (DRINCZ): validation and application to field-collected snow samples, Atmospheric Measurement Techniques, 12, 6865–6888, https://doi.org/10.5194/amt-12-6865-2019, 2019.

Dee, D. P., Uppala, S. M., Simmons, A. J., Berrisford, P., Poli, P., Kobayashi, S., Andrae, U., Balmaseda, M. A., Balsamo, G., Bauer,
P., Bechtold, P., Beljaars, A. C. M., van de Berg, L., Bidlot, J., Bormann, N., Delsol, C., Dragani, R., Fuentes, M., Geer, A. J., Haim-
520   berger, L., Healy, S. B., Hersbach, H., Hólm, E. V., Isaksen, L., Kållberg, P., Köhler, M., Matricardi, M., McNally, A. P., Monge-Sanz,
B. M., Morcrette, J.-J., Park, B.-K., Peubey, C., de Rosnay, P., Tavolato, C., Thépaut, J.-N., and Vitart, F.: The ERA-Interim reanalysis:
configuration and performance of the data assimilation system, Quarterly Journal of the Royal Meteorological Society, 137, 553–597,
https://doi.org/https://doi.org/10.1002/qj.828, 2011.

DeMott, P. J., Prenni, A. J., Liu, X., Kreidenweis, S. M., Petters, M. D., Twohy, C. H., Richardson, M. S., Eidhammer, T., and Rogers, D. C.:
525   Predicting global atmospheric ice nuclei distributions and their impacts on climate, Proceedings of the National Academy of Sciences,
107, 11 217–11 222, https://doi.org/10.1073/pnas.0910818107, 2010.

DeMott, P. J., Hill, T. C. J., McCluskey, C. S., Prather, K. A., Collins, D. B., Sullivan, R. C., Ruppel, M. J., Mason, R. H., Irish, V. E., Lee,
T., Hwang, C. Y., Rhee, T. S., Snider, J. R., McMeeking, G. R., Dhaniyala, S., Lewis, E. R., Wentzell, J. J. B., Abbatt, J., Lee, C., Sultana,
C. M., Ault, A. P., Axson, J. L., Martinez, M. D., Venero, I., Santos-Figueroa, G., Stokes, M. D., Deane, G. B., Mayol-Bracero, O. L.,
530   Grassian, V. H., Bertram, T. H., Bertram, A. K., Moffett, B. F., and Franc, G. D.: Sea spray aerosol as a unique source of ice nucleating
particles, Proceedings of the National Academy of Sciences, 113, 5797–5803, https://doi.org/10.1073/pnas.1514034112, 2016.

Eyring, V., Bony, S., Meehl, G. A., Senior, C. A., Stevens, B., Stouffer, R. J., and Taylor, K. E.: Overview of the Coupled Model
Intercomparison Project Phase 6 (CMIP6) experimental design and organization, Geoscientific Model Development, 9, 1937–1958,
https://doi.org/10.5194/gmd-9-1937-2016, 2016.

535   Findeisen, W.: Kolloid-meteorologische Vorgänge bei Neiderschlags-bildung., Meteor. Z, 55, 121–133, 1938.

Forster, P., Storelvmo, T., Armour, K., Collins, W., Dufresne, J.-L., Frame, D., Lunt, D., Mauritsen, T., Palmer, M., M.Watanabe, Wild, M.,
and Zhang, H.: The Earth's Energy Budget, Climate Feedbacks, and Climate Sensitivity, in: Climate Change 2021: The Physical Science
Basis. Contribution of Working Group I to the Sixth Assessment Report of the Intergovernmental Panel on Climate Change, edited by
Masson-Delmotte, V., Zhai, P., Pirani, A., Connors, S. L., Péan, C., Berger, S., Caud, N., Chen, Y., Goldfarb, L., Gomis, M. I., Huang,
540   M., Leitzell, K., Lonnoy, E., Matthews, J. B. R., Maycock, T. K., Waterfield, T., Yelekçi, O., Yu, R., and Zhou, B., Cambridge University
Press, 2021.

Geerts, B., Giangrande, S. E., McFarquhar, G. M., Xue, L., Abel, S. J., Comstock, J. M., Crewell, S., DeMott, P. J., Ebell, K., Field, P., Hill,
T. C. J., Hunzinger, A., Jensen, M. P., Johnson, K. L., Juliano, T. W., Kollias, P., Kosovic, B., Lackner, C., Luke, E., Lüpkes, C., Matthews,
A. A., Neggers, R., Ovchinnikov, M., Powers, H., Shupe, M. D., Spengler, T., Swanson, B. E., Tjernström, M., Theisen, A. K., Wales,
545   N. A., Wang, Y., Wendisch, M., and Wu, P.: The COMBLE Campaign: A Study of Marine Boundary Layer Clouds in Arctic Cold-Air
Outbreaks, Bulletin of the American Meteorological Society, 103, E1371 – E1389, https://doi.org/10.1175/BAMS-D-21-0044.1, 2022.

Gjelsvik, A. B.: Ice Nucleating Particles in Arctic Clouds and Their Impact on Climate, Master's thesis, University of Oslo, http://hdl.handle.
net/10852/95720, 2022.

Hahn, L. C., Armour, K. C., Zelinka, M. D., Bitz, C. M., and Donohoe, A.: Contributions to Polar Amplification in CMIP5 and CMIP6
550   Models, Frontiers in Earth Science, 9, https://doi.org/10.3389/feart.2021.710036, 2021.

Hersbach, H., Bell, B., Berrisford, P., Biavati, G., Horányi, A., Muñoz Sabater, J., Nicolas, J., Peubey, C., Radu, R., Rozum, I.,
Schepers, D., Simmons, A., Soci, C., Dee, D., and Thépaut, J.-N.: ERA5 hourly data on pressure levels from 1940 to present,
https://doi.org/10.24381/cds.bd0915c6, 2023.

Hoose, C., Kristjánsson, J. E., Chen, J.-P., and Hazra, A.: A Classical-Theory-Based Parameterization of Heterogeneous Ice Nucleation by Mineral Dust, Soot, and Biological Particles in a Global Climate Model, Journal of the Atmospheric Sciences, 67, 2483 – 2503, https://doi.org/10.1175/2010JAS3425.1, 2010.

Huang, W. T. K., Ickes, L., Tegen, I., Rinaldi, M., Ceburnis, D., and Lohmann, U.: Global relevance of marine organic aerosol as ice nucleating particles, Atmospheric Chemistry and Physics, 18, 11 423–11 445, https://doi.org/10.5194/acp-18-11423-2018, 2018.

Hurrell, J. W., Holland, M. M., Gent, P. R., Ghan, S., Kay, J. E., Kushner, P. J., Lamarque, J.-F., Large, W. G., Lawrence, D., Lindsay, K., Lipscomb, W. H., Long, M. C., Mahowald, N., Marsh, D. R., Neale, R. B., Rasch, P., Vavrus, S., Vertenstein, M., Bader, D., Collins, W. D., Hack, J. J., Kiehl, J., and Marshall, S.: The Community Earth System Model: A Framework for Collaborative Research, Bulletin of the American Meteorological Society, 94, 1339 – 1360, https://doi.org/10.1175/BAMS-D-12-00121.1, 2013.

Iversen, T., Bentsen, M., Bethke, I., Debernard, J. B., Kirkevåg, A., Seland, Ø., Drange, H., Kristjansson, J. E., Medhaug, I., Sand, M., and Seierstad, I. A.: The Norwegian Earth System Model, NorESM1-M – Part 2: Climate response and scenario projections, Geoscientific Model Development, 6, 389–415, https://doi.org/10.5194/gmd-6-389-2013, 2013.

Kanji, Z. A., Ladino, L. A., Wex, H., Boose, Y., Burkert-Kohn, M., Cziczo, D. J., and Krämer, M.: Overview of Ice Nucleating Particles, Meteorological Monographs, 58, 1.1 – 1.33, https://doi.org/10.1175/AMSMONOGRAPHS-D-16-0006.1, 2017.

Kanji, Z. A., Welti, A., Corbin, J. C., and Mensah, A. A.: Black Carbon Particles Do Not Matter for Immersion Mode Ice Nucleation, Geophysical Research Letters, 47, e2019GL086 764, https://doi.org/https://doi.org/10.1029/2019GL086764, e2019GL086764 2019GL086764, 2020.

Kartverket: Andenes map, http://norgeskart.no, accessed: 2022-04-26, 2022.

Kawai, K., Matsui, H., and Tobo, Y.: Dominant Role of Arctic Dust With High Ice Nucleating Ability in the Arctic Lower Troposphere, Geophysical Research Letters, 50, e2022GL102 470, https://doi.org/https://doi.org/10.1029/2022GL102470, e2022GL102470 2022GL102470, 2023.

Kirkevåg, A., Iversen, T., Seland, Ø., Hoose, C., Kristjánsson, J. E., Struthers, H., Ekman, A. M. L., Ghan, S., Griesfeller, J., Nilsson, E. D., and Schulz, M.: Aerosol–climate interactions in the Norwegian Earth System Model – NorESM1-M, Geoscientific Model Development, 6, 207–244, https://doi.org/10.5194/gmd-6-207-2013, 2013.

Kirkevåg, A., Grini, A., Olivié, D., Seland, Ø., Alterskjær, K., Hummel, M., Karset, I. H. H., Lewinschal, A., Liu, X., Makkonen, R., Bethke, I., Griesfeller, J., Schulz, M., and Iversen, T.: A production-tagged aerosol module for Earth system models, OsloAero5.3 – extensions and updates for CAM5.3-Oslo, Geoscientific Model Development, 11, 3945–3982, https://doi.org/10.5194/gmd-11-3945-2018, 2018.

Li, G., Wieder, J., Pasquier, J. T., Henneberger, J., and Kanji, Z. A.: Predicting atmospheric background number concentration of ice nucleating particles in the Arctic, Atmospheric Chemistry and Physics Discussions, 2022, 1–27, https://doi.org/10.5194/acp-2022-21, 2022.

Loeb, N. G., Doelling, D. R., Wang, H., Su, W., Nguyen, C., Corbett, J. G., Liang, L., Mitrescu, C., Rose, F. G., and Kato, S.: Clouds and the Earth's Radiant Energy System (CERES) Energy Balanced and Filled (EBAF) Top-of-Atmosphere (TOA) Edition-4.0 Data Product, Journal of Climate, 31, 895 – 918, https://doi.org/10.1175/JCLI-D-17-0208.1, 2018.

Maturilli, M.: Basic and other measurements of radiation at station Ny-Ålesund (2006-05 et seq), https://doi.org/10.1594/PANGAEA.914927, 2020.

McArthur, L.: Baseline Surface Radiation Network (BSRN). Operations Manual Version 2.1, https://bsrn.awi.de/fileadmin/user_upload/bsrn.awi.de/Publications/McArthur.pdf, 2005.

590 McCluskey, C. S., DeMott, P. J., Ma, P.-L., and Burrows, S. M.: Numerical Representations of Marine Ice-Nucleating Particles in Remote Marine Environments Evaluated Against Observations, Geophysical Research Letters, 46, 7838–7847, https://doi.org/https://doi.org/10.1029/2018GL081861, 2019.

Meyers, M. P., DeMott, P. J., and Cotton, W. R.: New Primary Ice-Nucleation Parameterizations in an Explicit Cloud Model, Journal of Applied Meteorology and Climatology, 31, 708 – 721, https://doi.org/10.1175/1520-0450(1992)031<0708:NPINPI>2.0.CO;2, 1992.

595 Miller, A. J., Brennan, K. P., Mignani, C., Wieder, J., David, R. O., and Borduas-Dedekind, N.: Development of the drop Freezing Ice Nuclei Counter (FINC), intercomparison of droplet freezing techniques, and use of soluble lignin as an atmospheric ice nucleation standard, Atmospheric Measurement Techniques, 14, 3131–3151, https://doi.org/10.5194/amt-14-3131-2021, 2021.

Morrison, H. and Gettelman, A.: A New Two-Moment Bulk Stratiform Cloud Microphysics Scheme in the Community Atmosphere Model, Version 3 (CAM3). Part I: Description and Numerical Tests, J. Clim., 21, 3642–3659, https://doi.org/10.1175/2008JCLI2105.1, 2008.

600 Murray, B. J., Carslaw, K. S., and Field, P. R.: Opinion: Cloud-phase climate feedback and the importance of ice-nucleating particles, Atmospheric Chemistry and Physics, 21, 665–679, https://doi.org/10.5194/acp-21-665-2021, 2021.

NASA: CERES_EBAF_Ed4.1 Data Quality Summary, https://ceres.larc.nasa.gov/documents/DQ_summaries/CERES_EBAF_Ed4.1_DQS.pdf, 2021.

Pereira Freitas, G., Adachi, K., Conen, F., Heslin-Rees, D., Krejci, R., Tobo, Y., Yttri, K. E., and Zieger, P.: Regionally sourced bioaerosols
605 drive high-temperature ice nucleating particles in the Arctic, Nature Communications, 14, 5997, https://doi.org/10.1038/s41467-023-41696-7, 2023.

Prenni, A. J., Harrington, J. Y., Tjernström, M., DeMott, P. J., Avramov, A., Long, C. N., Kreidenweis, S. M., Olsson, P. Q., and Verlinde, J.: Can Ice-Nucleating Aerosols Affect Arctic Seasonal Climate?, Bulletin of the American Meteorological Society, 88, 541 – 550, https://doi.org/10.1175/BAMS-88-4-541, 2007.

610 Rantanen, M., Karpechko, A., Lipponen, A., Nordling, K., Hyvärinen, O., Ruosteenoja, K., Vihma, T., and Laaksonen, A.: The Arctic has warmed four times faster than the globe since 1980, https://doi.org/https://doi.org/10.21203/rs.3.rs-654081/v1, pREPRINT (Version 1) available at Research Square, 2021.

Riihimaki, L., Long, C., and Dutton, E. G.: Basic and other measurements of radiation at station Barrow (1992-01 et seq), https://doi.org/10.1594/PANGAEA.959215, 2023.

615 Rogers, D. C.: Field and laboratory studies of ice nucleation in winter orogpahic clouds, University of Wyoming, 1982.

Schill, G. P., DeMott, P. J., Emerson, E. W., Rauker, A. M. C., Kodros, J. K., Suski, K. J., Hill, T. C. J., Levin, E. J. T., Pierce, J. R., Farmer, D. K., and Kreidenweis, S. M.: The contribution of black carbon to global ice nucleating particle concentrations relevant to mixed-phase clouds, Proceedings of the National Academy of Sciences, 117, 22 705–22 711, https://doi.org/10.1073/pnas.2001674117, 2020.

Seland, Ø., Bentsen, M., Olivié, D., Toniazzo, T., Gjermundsen, A., Graff, L. S., Debernard, J. B., Gupta, A. K., He, Y., Kirkevåg, A.,
620 Schwinger, J., Tjiputra, J., Aas, K. S., Bethke, I., Fan, Y., Gao, S., Griesfeller, J., Grini, A., Guo, C., Ilicak, M., Karset, I. H. H., Landgren, O., Liakka, J., Moree, A., Moseid, K. O., Nummelin, A., Spensberger, C., Tang, H., Zhang, Z., Heinze, C., Iversen, T., and Schulz, M.: NorESM2 source code as used for CMIP6 simulations (includes additional experimental setups, extended model documentation, automated inputdata download, restructuring of BLOM/iHAMOCC input data), https://doi.org/10.5281/zenodo.3905091, 2020a.

Seland, Ø., Bentsen, M., Olivié, D., Toniazzo, T., Gjermundsen, A., Graff, L. S., Debernard, J. B., Gupta, A. K., He, Y.-C., Kirkevåg,
625 A., Schwinger, J., Tjiputra, J., Aas, K. S., Bethke, I., Fan, Y., Griesfeller, J., Grini, A., Guo, C., Ilicak, M., Karset, I. H. H., Landgren, O., Liakka, J., Moseid, K. O., Nummelin, A., Spensberger, C., Tang, H., Zhang, Z., Heinze, C., Iversen, T., and Schulz, M.: Overview

of the Norwegian Earth System Model (NorESM2) and key climate response of CMIP6 DECK, historical, and scenario simulations, Geoscientific Model Development, 13, 6165–6200, https://doi.org/10.5194/gmd-13-6165-2020, 2020b.

Serreze, M. C. and Barry, R. G.: Processes and impacts of Arctic amplification: A research synthesis, Global and Planetary Change, 77,
630   85–96, https://doi.org/https://doi.org/10.1016/j.gloplacha.2011.03.004, 2011.

Shaw, J., McGraw, Z., Bruno, O., Storelvmo, T., and Hofer, S.: Using Satellite Observations to Evaluate Model Microphysical Representation of Arctic Mixed-Phase Clouds, Geophysical Research Letters, 49, e2021GL096191, https://doi.org/https://doi.org/10.1029/2021GL096191, e2021GL096191 2021GL096191, 2022.

Sprenger, M. and Wernli, H.: THE LAGRANTO Lagrangian analysis tool – version 2.0, Geoscientific Model Development, 8, 2569–2586,
635   https://doi.org/10.5194/gmd-8-2569-2015, 2015.

Stephens, G. L.: Radiation Profiles in Extended Water Clouds. II: Parameterization Schemes, Journal of Atmospheric Sciences, 35, 2123 – 2132, https://doi.org/10.1175/1520-0469(1978)035<2123:RPIEWC>2.0.CO;2, 1978.

Storelvmo, T. and Tan, I.: The Wegener-Bergeron-Findeisen process - Its discovery and vital importance for weather and climate, Meteorologische Zeitschrift, 24, 455–461, https://doi.org/10.1127/metz/2015/0626, 2015.

640   Sze, K. C. H., Wex, H., Hartmann, M., Skov, H., Massling, A., Villanueva, D., and Stratmann, F.: Ice-nucleating particles in northern Greenland: annual cycles, biological contribution and parameterizations, Atmospheric Chemistry and Physics, 23, 4741–4761, https://doi.org/10.5194/acp-23-4741-2023, 2023.

Tan, I. and Storelvmo, T.: Evidence of Strong Contributions From Mixed-Phase Clouds to Arctic Climate Change, Geophysical Research Letters, 46, 2894–2902, https://doi.org/https://doi.org/10.1029/2018GL081871, 2019.

645   Tan, I., Storelvmo, T., and Zelinka, M. D.: Observational constraints on mixed-phase clouds imply higher climate sensitivity, Science, 352, 224–227, https://doi.org/10.1126/science.aad5300, 2016.

Taylor, P. C., Boeke, R. C., Boisvert, L. N., Feldl, N., Henry, M., Huang, Y., Langen, P. L., Liu, W., Pithan, F., Sejas, S. A., and Tan, I.: Process Drivers, Inter-Model Spread, and the Path Forward: A Review of Amplified Arctic Warming, Frontiers in Earth Science, 9, https://doi.org/10.3389/feart.2021.758361, 2022.

650   Tobo, Y., Adachi, K., DeMott, P. J., Hill, T. C. J., Hamilton, D. S., Mahowald, N. M., Nagatsuka, N., Ohata, S., Uetake, J., Kondo, Y., and Koike, M.: Glacially sourced dust as a potentially significant source of ice nucleating particles, Nature Geoscience, 12, 253–258, https://doi.org/10.1038/s41561-019-0314-x, 2019.

Toniazzo, T., Bentsen, M., Craig, C., Eaton, B. E., Edwards, J., Goldhaber, S., Jablonowski, C., and Lauritzen, P. H.: Enforcing conservation of axial angular momentum in the atmospheric general circulation model CAM6, Geoscientific Model Development, 13, 685–705,
655   https://doi.org/10.5194/gmd-13-685-2020, 2020.

Vali, G.: Quantitative Evaluation of Experimental Results an the Heterogeneous Freezing Nucleation of Supercooled Liquids, Journal of the Atmospheric Sciences, 28, 402—-409, https://doi.org/https://doi.org/10.1175/1520-0469(1971)028<0402:QEOERA>2.0.CO;2, 1971.

Vergara-Temprado, J., Murray, B. J., Wilson, T. W., O'Sullivan, D., Browse, J., Pringle, K. J., Ardon-Dryer, K., Bertram, A. K., Burrows, S. M., Ceburnis, D., DeMott, P. J., Mason, R. H., O'Dowd, C. D., Rinaldi, M., and Carslaw, K. S.: Contribution of feldspar
660   and marine organic aerosols to global ice nucleating particle concentrations, Atmospheric Chemistry and Physics, 17, 3637–3658, https://doi.org/10.5194/acp-17-3637-2017, 2017.

Vergara-Temprado, J., Holden, M. A., Orton, T. R., O'Sullivan, D., Umo, N. S., Browse, J., Reddington, C., Baeza-Romero, M. T., Jones, J. M., Lea-Langton, A., Williams, A., Carslaw, K. S., and Murray, B. J.: Is Black Carbon an Unimportant Ice-Nucleating Particle in Mixed-

Phase Clouds?, Journal of Geophysical Research: Atmospheres, 123, 4273–4283, https://doi.org/https://doi.org/10.1002/2017JD027831, 2018.

Wegener, A.: Thermodynamik der Atmosphäre, 1911.

Westbrook, C. and Illingworth, A.: The formation of ice in a long-lived supercooled layer cloud, Q.J.R. Meteorol. Soc, 139, 2209–2221, https://doi.org/https://doi.org/10.1002/qj.2096, 2013.

Wex, H., Huang, L., Zhang, W., Hung, H., Traversi, R., Becagli, S., Sheesley, R. J., Moffett, C. E., Barrett, T. E., Bossi, R., Skov, H., Hünerbein, A., Lubitz, J., Löffler, M., Linke, O., Hartmann, M., Herenz, P., and Stratmann, F.: Annual variability of ice-nucleating particle concentrations at different Arctic locations, Atmospheric Chemistry and Physics, 19, 5293–5311, https://doi.org/10.5194/acp-19-5293-2019, 2019.

Winker, D. M., Vaughan, M. A., Omar, A., Hu, Y., Powell, K. A., Liu, Z., Hunt, W. H., and Young, S. A.: Overview of the CALIPSO Mission and CALIOP Data Processing Algorithms, Journal of Atmospheric and Oceanic Technology, 26, 2310 – 2323, https://doi.org/10.1175/2009JTECHA1281.1, 2009.

Xie, S., Liu, X., Zhao, C., and Zhang, Y.: Impact of ice nucleation parameterizations on CAM5 simulated arctic clouds and radiation: A sensitivity study, AIP Conference Proceedings, 1527, 747–750, https://doi.org/10.1063/1.4803378, 2013.

Young, K. C.: The Role of Contact Nucleation in Ice Phase Initiation in Clouds, Journal of Atmospheric Sciences, 31, 768 – 776, https://doi.org/10.1175/1520-0469(1974)031<0768:TROCNI>2.0.CO;2, 1974.

Yun, Y. and Penner, J. E.: An evaluation of the potential radiative forcing and climatic impact of marine organic aerosols as heterogeneous ice nuclei, Geophysical Research Letters, 40, 4121–4126, https://doi.org/https://doi.org/10.1002/grl.50794, 2013.

Zelinka, M. D., Myers, T. A., McCoy, D. T., Po-Chedley, S., Caldwell, P. M., Ceppi, P., Klein, S. A., and Taylor, K. E.: Causes of Higher Climate Sensitivity in CMIP6 Models, Geophysical Research Letters, 47, e2019GL085 782, https://doi.org/https://doi.org/10.1029/2019GL085782, e2019GL085782 10.1029/2019GL085782, 2020.

Zhao, X., Liu, X., Burrows, S. M., and Shi, Y.: Effects of marine organic aerosols as sources of immersion-mode ice-nucleating particles on high-latitude mixed-phase clouds, Atmospheric Chemistry and Physics, 21, 2305–2327, https://doi.org/10.5194/acp-21-2305-2021, 2021.